

Faculdade de Engenharia da Universidade do Porto



FEUP

**Laser scanning system for 3D modelling of
prostheses inner surface**

Frederico Alberto de Abreu Carpinteiro

Dissertation
Integrated Master in Bioengineering
Major in Biomedical Engineering

Supervised by:
Professor Miguel Fernando Paiva Velhote Correia (FEUP)
Filipe Tiago Alves de Magalhães, PhD

<19 June 2014>

“When you have a disability,
knowing that you are not defined by it
is the sweetest feeling.”
In My Dreams I Dance, Anne Wafula Strike

Abstract

The main goal of the work was the development of a laser scanning system for 3D modelling of the inner surface of a lower limb prosthesis socket, in order to allow the evaluation of the adaptation between the socket and the patient stump.

The need for the creation of a system of this type appeared from the lack of adaptation between the prostheses sockets and the amputees' stumps, which leads to a great number of replacements and rejections of prostheses.

After the assessment of the specificities presented by the problem and by the features of the sockets, as well of the different methods to perform 3D measurements, it was decided to develop a system based on active light for laser scanning. Considering the relation between simplicity/availability to get the needed materials, the performance possible to obtain with this system, and its adequacy to the restrictions placed by the object of study, laser scanning showed to be the best approach.

For the development of the system it was needed to design and implement a mechanical part capable of scanning with stability along the z axis, while maintaining the linkage of the optical part during the entire scanning process. To control the mechanical part, a step motor was used, and to control the motor an electronic circuit connected to a PC was projected and assembled. An algorithm to control the system using Matlab was also developed.

The developed system projects a circular laser line on different z-positions of the object, with a user defined step between them. Two algorithms for the segmentation of the projected laser line were developed, tested and compared, thus allowing to identify the one with best performance. The points extracted from its segmentation were used to create a point cloud that could be exported to 3D mesh processing software, such as Meshlab, thus allowing its manipulation and creation of a final 3D model.

To evaluate the system, 3D models of known shape objects were built, as well as the 3D model of a leg prosthesis socket, which was the main goal of this work.

The obtained models allowed to determine that the average measurement error was 1.04 ± 0.37 mm which is acceptable once the dimensional variation of the amputee's stump is in the 10 mm range.

Resumo

O objetivo principal deste trabalho foi o desenvolvimento de um sistema de varrimento laser para modelação 3D da superfície interior do encaixe de próteses do membro inferior, para permitir a avaliação da adaptação entre o encaixe e o coto do paciente.

A necessidade da criação de um sistema deste tipo surgiu da falta de adaptação verificada entre os encaixes das próteses e os cotos dos amputados, levando a um grande número de substituições e rejeições de próteses.

Após uma avaliação das especificidades apresentadas pelo problema e pelas características dos encaixes, bem como dos diferentes métodos usados para realizar medições tridimensionais, foi decidido desenvolver um sistema baseado em luz ativa para varrimento laser. Considerando a relação entre simplicidade/disponibilidade para obter os materiais necessários, a performance possível de obter com um sistema deste tipo, e a sua adequação às restrições apresentadas pelo objecto de análise, o varrimento laser mostrou ser a melhor abordagem a seguir.

Para o desenvolvimento do sistema foi necessário desenhar e implementar uma peça mecânica capaz de realizar o deslocamento ao longo do eixo z com estabilidade, mantendo ao mesmo tempo o alinhamento da parte ótica do sistema durante todo o processo de varrimento. Para controlar a parte mecânica do sistema, foi usado um motor de passo, e para controlar esse motor um circuito electrónico conectado com um PC foi desenhado e implementado. Também foi desenvolvido um algoritmo para controlar todo o sistema a partir do Matlab.

O sistema desenvolvido projeta uma linha laser circular em diferentes posições em z do objecto, com um espaçamento definido pelo utilizador entre elas. Foram desenvolvidos, testados e comparados dois algoritmos para a segmentação da linha laser projetada para identificar o que teria a melhor performance. Os pontos extraídos da linha segmentada foram usados para criar uma nuvem de pontos que pode ser exportada para um software de processamento tridimensional de malhas, como por exemplo o MeshLab, permitindo a criação e manipulação do modelo 3D final.

Para avaliar o sistema, foram criados modelos 3D de objetos de forma conhecida, bem como o modelo tridimensional de um encaixe de uma prótese do membro inferior, que era o objectivo principal deste trabalho. Os modelos obtidos permitiram determinar que o erro médio foi de 1.04 ± 0.37 mm, o que se trata de um valor aceitável uma vez que a variação dimensional do coto do amputado durante um dia é na ordem dos 10 mm.

Acknowledgments

For the success of the performed work, the contribution of several people was very important.

First of all I would like to thanks to mechanical engineering student João Martins and to Professor Francisco Xavier de Carvalho from Design Studio (FEUP) for the important help in designing and projecting the mechanical system for the needed function, and to Motofil Robotics SA and MICOM for providing the needed materials and produce the designed mechanical system.

I would also like to thanks to Engineer Nuno Sousa from Departamento de Engenharia Eletrotécnica e de Computadores da Faculdade de Engenharia do Porto, for the great availability and help in designing the electronic circuit to control the stepping motor.

To my supervisors Professor Miguel Fernando Paiva Velhote Correia and PhD Filipe Tiago Alves de Magalhães for all the guiding and availability they provided, I'm very grateful.

To my parents for all the love and support, and for providing everything I needed and more during these 5 years, I would like to express my deepest gratitude.

To Liliana I want to thank for always being there for me.

At last I would like to thank to INESC Porto and Departamento de Engenharia Eletrotécnica e de Computadores da Faculdade de Engenharia do Porto for the materials, facilities and funding provided so far, that proved to be crucial for the development of the work.

Index

Abstract	v
Resumo	vii
Acknowledgments	ix
Index	xi
Figure List	xiii
Table List	xvii
Abbreviations and Symbols	xix
Glossary	xxi
Medical	xxi
Technical	xxi
Chapter 1	1
Introduction	1
1.1 - Motivation	1
1.2 - Objectives.....	2
1.3 - Contributions	2
1.4 - Publications.....	2
1.5 - Structure	3
Chapter 2	5
The Problematic of Lower Limb Protheses	5
2.1 - The Lower Limb	5
2.2 - Amputation and Causes	6
2.3 - Post-Chirurgical Management	8
2.4 - Summary	18
Chapter 3	19
3D Modelling - methodologies and applications.....	19
3.1 - 3D Measurements	19
3.2 - 3D Reconstruction and Modelling.....	25
3.3 - Prosthesis 3D Modelling	28
3.4 - Summary	30

Chapter 4	31
Laser Scanning System	31
4.1 - System Design and Implementation.....	31
4.2 - Experimental Procedure	35
4.3 - User Interface	39
4.4 - Summary	40
Chapter 5	41
Image Processing Algorithms for Segmentation of the Circular Laser Line	41
5.1 - Methodology	41
5.2 - Results.....	46
5.3 - Summary	50
Chapter 6	51
System Calibration and Characterization	51
6.1 - System Calibration.....	51
6.2 - System Characterization.....	53
6.3 - Summary	61
Chapter 7	63
3D Model Reconstruction	63
7.1 - Methodology	63
7.2 - Results.....	65
7.3 - Summary	68
Chapter 8	69
Conclusions	69
Appendixes	71
I. Mechanical System Technical Drawings	72
II. Electronic Circuit for Step Motor Control	81
References	83

Figure List

Figure 2.1 - Levels of lower limb amputation [8].	7
Figure 2.2 - Examples of initial (left) and preparatory (right) lower limb prostheses [8].	9
Figure 2.3 - Examples of modular (A) and traditional (B) definitive transfemoral prosthesis; examples of modular (C) and traditional (D) definitive transtibial prosthesis [8].	10
Figure 2.4 - Examples of special-use prosthesis for running (left) or skiing (right) [8].	10
Figure 2.5 - Example of a exoskeletal wood prosthesis [13].	11
Figure 2.6 - Endoskeletal prosthesis for above knee amputation [13].	12
Figure 2.7 - Lower limb prosthesis components [13].	12
Figure 2.8 - Stump measurement for volumetric reproduction [13].	13
Figure 2.9 - (a) Plaster application on the stump, (b) Obtained mold for plaster filling [13].	13
Figure 2.10 - (a) Mold filling, (b) Stump plaster replica obtained [13].	14
Figure 2.11 - (a) Dimensional verification of the stump replica [13].	14
Figure 2.12 - Final result after adjustments [13].	14
Figure 2.13 - Socket prototype in polypropylene [13].	15
Figure 2.14 - (a) First test of the socket by the patient, (b) Verification of the contact zone [13].	15
Figure 2.15 - Finishing the final socket with a termoplastic material [13].	16
Figure 2.16 - Different types of sockets.	17
Figure 3.1 - Organization tree of 3D measurement methods for shape acquisition.	19
Figure 3.2 - Organization tree of optical methods used for 3D measurements.	20
Figure 3.3 - Image formation with lenses: all the light rays coming from a point P in the focal plane are projected into a single point p in the image plane [20].	22
Figure 4.1 - Scheme depicting the laser scanning principle along the z-axis.	31
Figure 4.2 - Principle of sample analysis and model reconstruction.	32
Figure 4.3 - Main components of the developed scanning system.	32

Figure 4.4 - Main components of the developed mechanical system that enable it to perform the movement along the z axis.....	33
Figure 4.5 - System in the highest position.....	35
Figure 4.6 - Alignment of the object with the system.....	36
Figure 4.7 - Alignment of the prosthesis socket with the system.....	37
Figure 4.8 - Complete scanning (two directions with rotation).	38
Figure 4.9 - Developed user interface, for system control and result analysis.	39
Figure 5.1 - Example of an image acquired by the scanning system (original RGB image)....	42
Figure 5.2 - Red component of the previous RGB image.	42
Figure 5.3 - Detected center in the acquired image, with a zoom on the right.	42
Figure 5.4 - Example of an acquired image by the developed system in polar coordinates. .	43
Figure 5.5 - New polar image containing in each column either the detected maximum in the position it was detected or the data from the original image (on the top), with a zoom of the selected area (below).....	43
Figure 5.6 - Area of the image discarded from the analysis corresponding to the physical space occupied by the laser support.....	44
Figure 5.7 - Minimum path resulting from the MIMP algorithm.....	44
Figure 5.8 - Segmented circular laser line resulting from the MIMP algorithm.	44
Figure 5.9 - Positive gradient image resulting from the original polar image.....	45
Figure 5.10 - Negative gradient image resulting from the original polar image.....	45
Figure 5.11 - New polar image containing in each column either the maximum detected, in the average position of the maximum in the two gradient images, or the data from the original polar image (on the top), with a zoom of the selected area (below).	45
Figure 5.12 - Minimum path resulting from the GAMP algorithm.	45
Figure 5.13 - Segmented circular laser line resulting from the MIMP algorithm.....	46
Figure 5.14 - Real Image (circular line generated with the results of the manual measurements of the object).	47
Figure 5.15 - Image in which the ground truth was marked (left) and marked ground truth (right).	47
Figure 5.16 - Socket image where the ground truth was marked (left) and marked ground truth (right).	49
Figure 6.1 - Setup used for calibration of the system (left), grid image acquired with the system camera (center) and a zoomed scheme of the used grid (right).	51
Figure 6.2 - System calibration evaluation.	52

Figure 6.3 - Data used to perform the system calibration, with the scheme of an inset on the right.	53
Figure 6.4 - Dark cone with a diameter between 80 and 130.5 mm, used for the system characterization tests.	53
Figure 6.5 - System linearity graph.	54
Figure 6.6 - System resolution graph.	55
Figure 6.7 - System reproducibility graph.....	56
Figure 6.8 - Variation of the z-position of the system inside the cone for the accuracy test.	57
Figure 6.9 - Error (Real to Virtual) obtained for the acquired images for the random dislocations of the system.	58
Figure 6.10 - Error (Virtual to Real) obtained for the acquired images for the random dislocations of the system.	58
Figure 6.11 - Variation of the z-position of the system for the movement accuracy test.....	59
Figure 6.12 - Experimental assembly with the system and the used precision ruler for the movement accuracy test.	60
Figure 6.13 - Movement error on the performed random system movements.	60
Figure 7.1 - Photos from two different views of the PVC dark grey tube with 121.2 mm diameter that was used in the scanning experiments.	64
Figure 7.2 - Point Cloud representing the scanned tube, visualized in MeshLab.	64
Figure 7.3 - Two different views of the initial 3D model (unedited triangular mesh) of the tube represented in Figure 7.1	65
Figure 7.4 - Triangular mesh edition (faces erasing) in MeshLab.	65
Figure 7.5 - 3D models resulting from the system measurements: triangular mesh model and solid model.....	66
Figure 7.6 - 3D models resulting from the manual measurements: triangular mesh model and solid model.....	66
Figure 7.7 - Photos from two different views of the socket used to test the 3D laser scanning system.	67
Figure 7.8 - 3D model of the scanned socket, in grey the triangular mesh from two different views and in black the solid model.	67
Figure I.1 - Technical drawing of the full mechanical system.	72
Figure I.2 - Technical drawing of the part that allows the movement along the x axis.	73
Figure I.3 - Technical drawing of the part that allows the shifting of the camera orientation.	74
Figure I.4 - Technical drawing of the guiding bars for the movement along z axis.....	75

Figure I.5 - Technical drawing of the supporting part.	76
Figure I.6 - Technical drawing of the part that supports the laser.	77
Figure I.7 - Technical drawing of the part that supports the conic mirror.	78
Figure I.8 - Technical drawing of the part that allows the mount of the mechanical system to a vertical surface.	79
Figure I.9 - Technical drawing of the part that supports the spindle.....	80
Figure II.1 - Electronic circuit developed for step motor control.	81

Table List

Table I: Prosthetic CAD/CAM systems available in the market (AK=Above Knee, BK=Below knee) [8]	29
Table II: Specifications of the laser scanning system components	34
Table III: System specifications	35
Table IV: Segmentation error relatively to the real image	47
Table V: Segmentation error relatively to the ground truth.....	48
Table VI: Error between the marked ground truth and the real image.....	48
Table VII: Algorithm processing time.....	48
Table VIII: System error relatively to the marked ground truth, in the prosthesis socket.....	49
Table IX: Results for system resolution	55
Table X: Results of system reproducibility on the first 1000 samples.....	56
Table XI: Results of system reproducibility on the last 1000 samples	57

Abbreviations and Symbols

Abbreviations List

AK	Above Knee
BK	Below Knee
CAD	<i>Computer Aided Design</i>
CRPG	Centro de Reabilitação Profissional de Gaia
CT	Computerized Tomography
FEUP	Faculdade de Engenharia da Universidade do Porto
MRI	Magnetic Resonance Imaging
3D	Tridimensional
RGB	Red, Green, Blue

Glossary

Medical

- **Ischium** - the inferior dorsal portion of the hip bone [1]
- **Prosthesis** - an artificial substitute for a missing body part, such as an arm, leg, eye, or tooth; used for functional or cosmetic reasons, or both [1]
- **Socket** - The prosthetic socket joins your residual limb to the prosthesis and fulfills an important function: it ensures optimum adhesion and the proper fit of your prosthesis [2]
- **Stump** - the distal end of a limb left after amputation [1]

Technical

- **Breakline** - feature line or polyline representing a ridge or some feature that the user wishes to preserve in a mesh made up of polygonal elements [3]
- **Mesh** - it is a collection of triangular (or quadrilateral) contiguous, non-overlapping faces joined together along their edges. A mesh therefore contains vertices, edges and faces and its easiest representation is a single face [3]
- **Modeling** - the (mathematical) construction and computer implementation of an object, by defining points in a 3 dimensional array [3]
- **Simplices** - A Euclidean geometric spatial element having the minimum number of boundary points, such as a line segment in one-dimensional space, a triangle in two-dimensional space, or a tetrahedron in three-dimensional space [4]
- **Splines** - A piecewise polynomial function that can have a locally very simple form but at the same time be globally flexible and smooth. Splines are very useful for modeling arbitrary functions. A class of parametric curves and surfaces is the Non-Uniform Rational B-Spline (NURBS) curve or surface. They are the generalization of

non-rational B-splines, which are basis of polynomial function based on rational Bézier curves [3]

- **Surface** - a compact, connected, orientable 2D or 3D manifold, possibly with boundary [3]

Chapter 1

Introduction

1.1 - Motivation

The accurate number of amputees worldwide is unknown, but it is estimated to range between 10 and 20 million people.

Depending on the country health system, on the amputee financial capacity, and several different factors, like post-op recovery and stump configuration, different patients receive different prostheses, ones more common and simple and others more technologically complex. Despite of that, all the amputees of the lower limb share a common problem: the lack of adaptation.

This lack of adaptation is caused by the variability of the fabrication process and by the subjectivity associated with the evaluation of its adaptation to the user. The subjectivity of the process and evaluation is due to the great level of manual intervention, the lack of technological aid in this part of the process and to the reduced number of technologies that allow a complete study of the stump-prosthesis interface.

The adaptation of the amputee to its prosthesis is essential, once the lower limb prosthesis has to support most of the body weight, and the discomfort caused by the pressure felt in the interface can lead to the full rejection of the prosthesis by some users.

Nowadays, there are already some methods to perform the 3D modelling of the stump, but few are known to perform the 3D modelling of the inner surface of the prosthesis socket. The small number of methods to perform this kind of 3D modelling and the low resolution of the existing ones are caused by the difficulties presented by the object of study. Typically the socket subjected to this type of analysis presents a cylindrical form with relatively small dimensions and only one opening.

Since the existence of a high resolution and highly accurate method for the 3D modelling of the inner surface of the prosthesis socket is really important for a better study of the adaptation of an amputee to its prosthesis, the opportunity for this project emerged.

The future development of a system capable of performing a complete and optimized study of the stump-prosthesis interface, will allow the production of prostheses with a maximum level of adaptation of the amputee to its prosthesis and an easier optimization of the already existent prosthesis, giving him comfort and the opportunity to live a better life.

1.2 - Objectives

For the this thesis the following objectives were defined:

- Development of a laser scanning system for 3D modelling of leg prostheses socket inner surface;
- Complete characterization of the developed system;
- Development and implementation of a method for system calibration;
- Development of image processing and analysis algorithms in order to analyse the images acquired by the system, to detect and segment the projected circular laser line;
- Building a 3D model of a leg prosthesis socket interior with the geometrical information from the segmented lines;
- Development of a user interface (software) to manipulate the system;
- System test with an amputee.

1.3 - Contributions

1. Implementation of a circuit and associated software to control a step motor with PC.
2. Design, production and mount of a mechanical system to perform the scanning along the z axis.

1.4 - Publications

F. Carpinteiro, P. Costa, H. P. Oliveira, and F. Magalhães, "3D Models for Leg Prosthesis", StudECE 2012 - 1ST PhD. Students Conference in Eletrical and Computer Engineering, Porto, 28th-29th June, 2012

Out of the scope of this thesis:

F. A. Carpinteiro, P. M. Costa, M.S. Espinoza, I.M. Silva and João P.S. Cunha, "NeuronDynamics: a Method for Neurotransmitter Vesicle Movement Characterization in Neurons," IEEE International Symposium in Biomedical Imaging (ISBI 2014); Beijing, China; in press, 2014.

1.5 - Structure

This thesis is divided in 8 main chapters:

- **Chapter 1**, the present chapter, describes thesis objectives, structure and motivation.
- **Chapter 2** presents the problematic of lower limb prostheses from a medical perspective.
- **Chapter 3** presents the main techniques to perform 3D measurements and 3D visualization, and the techniques used in 3D modelling of prostheses.
- **Chapter 4** describes the developed system, by presenting a full set of specifications. This chapter also explains the experimental procedure of acquiring the data from the objects and the developed user interface.
- **Chapter 5** explains the methodology followed to perform the segmentation of the gathered images, and presents its results.
- **Chapter 6** explains how the calibration of the system was performed and its results, and presents a complete characterization of the system.
- **Chapter 7** explains the approach followed to obtain the reconstructed 3D models and the results obtained.
- **Chapter 8** ends the thesis with some concluding notes and presents future work.

Additionally, it contains two appendixes with the mechanical system technical drawings and the electronic circuit for stepper motor control.

Chapter 2

The Problematic of Lower Limb Prostheses

This chapter describes the problem of the amputation and the use of prostheses from a medical perspective, listing the main causes of amputation and the prostheses constitution, types and stages of use. The process of prostheses manufacturing and the concerns about stump-socket fitting are also discussed.

2.1 - The Lower Limb

The Lower Limb is an anatomical functional unit with several fundamental functions: static support (bipedalism), dynamic support (walk, run...), impact damping, among others [5]. Its functions suppose great mobility, articulation stability and a good alignment between segments and articulations.

According to Mendes, E. [5], the Lower Limb is composed by:

- Distal zone or ankle unit: foot, specialized in the transmission of forces from and for the ground;
- Proximal zone or pelvic girdle: specialized in the transmission of body weight to the terminal zone and in enabling movements like sitting;
- Medial zone: knee, controls the movements in the several plans and increases the efficiency of walk.

2.2 - Amputation and Causes

Lower-extremity amputations may be performed because of the following reasons [5-8]:

- **Peripheral vascular disease (PVD) - 75%:** most amputations performed are caused by ischemic disease, primarily in elderly persons with diabetes mellitus. These patients often experience peripheral neuropathy that progresses to trophic ulcers and subsequent gangrene and osteomyelitis;
- **Trauma - 12%:** severe open fractures with popliteal artery and posterior tibial nerve injuries can be treated with current techniques; however, treatment is at a high cost, and multiple surgeries are required. The result is often a leg that is painful, non-functional, and less efficient than a prosthesis;
- **Tumours - 5%:** Amputation is performed less frequently with the advent of advanced limb salvage techniques;
- **Nervous lesions - 6%:** reduction or loss of sensibility of a limb;
- **Congenital limb deficiency - 2%:** amputations for congenital limb deficiencies are performed primarily in the paediatric population because of failure of partial or complete formation of a portion of the limb;
- **Infections:** treatment of sepsis with vasoconstrictor agents may at times lead to vessel occlusion and subsequent extremity necrosis, necessitating amputation. At other times, eradication of infection from many difficult sources necessitates removal of the affected digit or limbs.

The resulting limb of an amputation is called stump. The higher the level of a lower limb amputation, the greater the energy expenditure that is required for walking. The levels of amputation are represented in **Figure 2.1** [9]. As the level of the amputation moves proximally, the walking speed of the individual decreases, and the oxygen consumption increases.

The amputation level is generally decided by the doctor based on the location of the amputation and its associated needs. It should always be located as most distal as possible so it facilitates the manufacturing of the prosthesis from a technical point of view. It is important to try to maintain the rebounds and to keep as most bone as possible to facilitate the fixation and the use of movements from the stump [10].

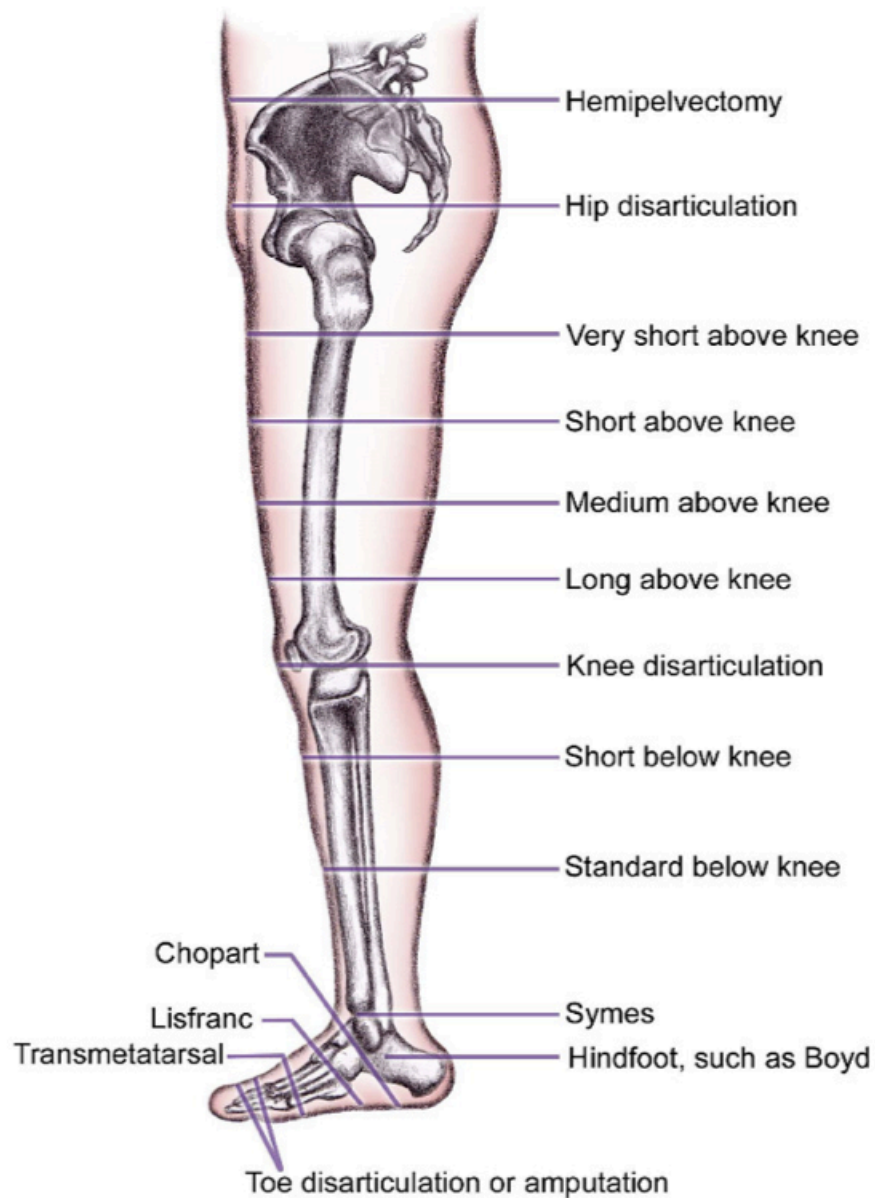


Figure 2.1 - Levels of lower limb amputation [8].

The amputation levels are classified and chosen with the purpose of allowing a complete healing and a good functionality of the limb after the rehabilitation process. The general state of the patient, its age, the coexistence of associated diseases, the surgical risk and the clinical context where the ischemia is verified are also determining factors of the urgency and choice of the amputation level [11].

2.3 - Post-Chirurgical Management

When amputation of a limb is being considered, it is important to inform the patient about future rehabilitation [12]. Different stages of the rehabilitation process, including how long the preparatory prosthesis will be used and when the evaluation for a definitive prosthesis will occur, will be defined accordingly to the patient.

2.3.1 - Prosthesis stages

There are four generic post-surgical stages [12]: postoperative, initial, preparatory and definitive or special-purpose prostheses. Although progression through all four levels may be desirable, not all the patients pass through them.

According to Gabbiadini, Stella [8], in detail the previously referred types of prostheses are:

1. Postoperative prosthesis: postoperative prostheses are, by definition, provided within 24 hours of amputation. These are often referred to by various acronyms including immediate postsurgical fitting (IPSF) and immediate postoperative prosthesis (IPOP). Although technically feasible for virtually any amputation, postoperative fittings are currently most commonly prescribed for the younger, healthier individual undergoing amputation due to tumour, trauma, or infection. Its use in the elderly individual is controversial but can be successful when meticulous technique and close supervision are available;

2. Initial prosthesis: the initial prosthesis (see example in **Figure 2.2**) is sometimes used instead of a postsurgical fitting and is provided as soon as the sutures are removed. This is sometimes referred to as an early postsurgical fitting (EPSF). Due to the usual rapid atrophy of the residual limb, the EPSF is generally directly moulded on the residual limb by using plaster or fiberglass bandages. An alternative is to use a weight-bearing rigid dressing. Such devices are used during the acute phase of healing, generally from 1 to 4 weeks after amputation, until the suture line is stable and the skin can tolerate the stresses of more intimate fitting. Postoperative and initial prostheses are most commonly used in rehabilitation units or in hospitals with very active amputee programs;

3. Preparatory prosthesis: this type of prosthesis (see example in **Figure 2.2**) is used during the first few months of the patient rehabilitation to ease the transition into a definitive device. They are also used in marginal cases to assess ambulatory or rehabilitation potential and help clarify details of the prosthetic prescription. The preparatory prosthesis accelerates rehabilitation by allowing ambulation before the residual limb has completely matured. Preparatory prostheses may be applied within a few days following suture or staple removal,

and limited gait training is started at that point. Originally, the preparatory prosthesis was a very rudimentary design containing only primitive components. The modern preparatory artificial limb, however, usually incorporates definitive-quality endoskeletal componentry but lacks the protective and cosmetic outer finishing to reduce the cost. It allows the therapist and prosthetist to work together to optimize alignment as the amputee gait pattern matures. Different types of knee mechanisms or other components can be tested to see whether individual patient function is improved. Preparatory prostheses are generally used for a period of 3 to 6 months following the date of amputation, but that time can vary depending on the speed of maturation of the residual limb and on other factors such as weight gain, weight loss, or health problems. The new amputee may begin by wearing one thin prosthetic sock in the preparatory prosthesis; after 3 months, he may be wearing ten plies of prosthetic socks to compensate for atrophy. When the number of plies of prosthetic socks the patient must wear remains stable over several weeks, it is usually an indication that the definitive prosthesis can be prescribed;



Figure 2.2 - Examples of initial (left) and preparatory (right) lower limb prostheses [8].

4. Definitive prosthesis: the definitive prosthesis should not be prescribed until the patient residual limb has stabilized to ensure that the fit of the new prosthesis will last as long as possible. The definitive prescription is based primarily upon the experience the patient had when using the preparatory prosthesis. The information learned during those months will demonstrate to the clinic team the patient's need for a lightweight design, special types of feet or suspension, or any special weight-bearing structure. There are mainly two kinds of definitive prosthesis: a traditional and a modular prostheses (see examples in **Figure 2.3**). The first type has rigid parts with the main function of supporting the bodyweight and aesthetically substitute a limb. They are usually made of wood or millwork resins. The second type has a supporting structure, which is tubular and modular, and it can have an external aesthetic soft cover. The use of modular prostheses in the last years has quickly increased, due to their extensive adaptability to different types of amputees and to the

possibility of substituting each single module of the prosthesis while maintaining all the others. For these reasons the use and the manufacturing of traditional prosthesis is slowly disappearing.

Unfortunately a definitive prosthesis is not for life. Due to its extended solicitation it will wear out like any other mechanical device. The average life span for a definitive prosthesis ranges from 3 to 5 years. Most are replaced due to changes in the amputee residual limb from atrophy, weight gain, or weight loss. Substantial changes in the amputee life-style or activities may also dictate a change in the prosthetic prescription. Overall physical condition is also a factor since the more debilitated individual generally requires a very lightweight and stable prosthesis.

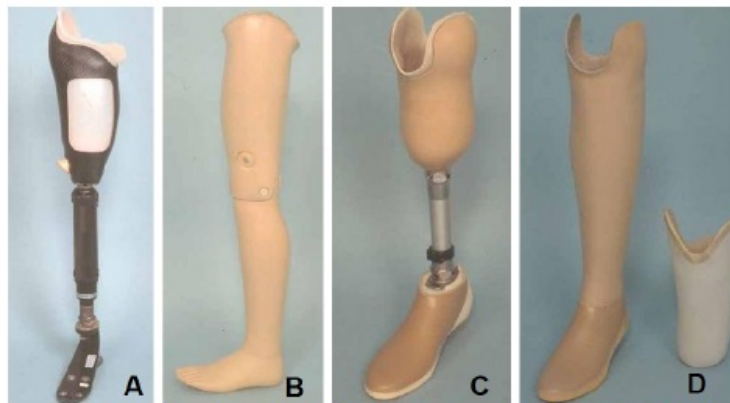


Figure 2.3 - Examples of modular (A) and traditional (B) definitive transfemoral prosthesis; examples of modular (C) and traditional (D) definitive transtibial prosthesis [8].

A certain number of patients will require special-use prostheses (see examples in **Figure 2.4**) designed specifically for activities such as showering, swimming, or skiing. It is most economical if special-use devices are prescribed at the same time as a definitive device since both can be fabricated from the same positive model. Also most of the special-use prostheses require specialized alignment, and can be valuable to the amputee who wishes to expand his activities and participate in a full range of sports and recreational activities.



Figure 2.4 - Examples of special-use prosthesis for running (left) or skiing (right) [8].

For the purpose of this work the definitive prostheses are those in which focus will be placed. The procedures to manufacture/assemble postoperative, initial and preparatory prostheses are quite simple, fast and standardized since these are temporary prostheses whose components have a short useful life and are reused for different amputees. The process to produce a definitive prosthesis is more elaborate and time-consuming since it has to perfectly custom-fit on the patient and it has a mean life of 3-5 years.

2.3.2 - Prosthesis types and components

Prostheses can firstly be divided into external, whose main function is to replace an amputated limb as a leg, and internal, that are introduced into the body, like the hip prosthesis [13]. The external prostheses can be divided into 2 new categories, accordingly to its characteristics: endoskeletal and exoskeletal prostheses [14]. The exoskeletal prostheses (**Figure 2.5**) are known as conventional prostheses, and are manufactured with wood or plastic. These materials do the connection between the socket and the foot of the prosthesis. The use of these materials can be availed to produce a pleasant aesthetic finishing, besides being the structural element that supports the entire body weight. This type of prostheses has the advantage of not needing a high maintenance when compared to other types, but it presents alignment problems and it is limited (movement, resistance, flexibility...) for some more demanding activities, such as running and lifting weights [13].



Figure 2.5 - Example of a exoskeletal wood prosthesis [13].

The endoskeletal prostheses (**Figure 2.6**) represent the modular prostheses, where the connection between the socket and the foot is made by modular components and tubes, which leads to the use of foam and cosmetic sock as aesthetic finishing. This configuration allows multiple types of conformations at performance level, and has consequences at economic level, which made them superior and the most used when compared to the conventional prostheses. The alignment and tension corrections can be directly adjusted in each component through screws and regulators, allowing a greater comfort and stability to the amputee [13].



Figure 2.6 - Endoskeletal prosthesis for above knee amputation [13].

The prosthesis main goal is the replacement of the absent limb, performing its functions. The prosthesis must be adapted accordingly to: age, gender, pathology, weight, height, morphology, expectations and lifestyle [5].

The modular type of lower limb prosthesis is composed as showed in the scheme of Figure 2.7: a socket, a knee (only for transfemoral patients), a tube, a foot and different typologies of locks and joints to assemble the various modules[8].

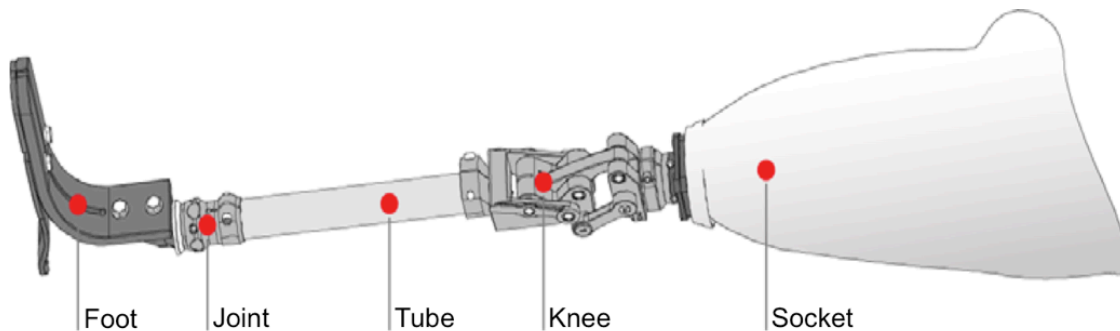


Figure 2.7 - Lower limb prosthesis components [13].

Independently of the amputation level, the socket is considered to be the most important part of a prosthesis. The socket shall fix the prosthesis to the residual limb of the patient, involve the stump without interfering with the blood circulation, transmit forces and control movements. Different levels of amputation lead to different needs and, as a consequence, to different sockets. Pressure points for fixation, weight discharge and prosthesis suspension should be defined for each patient, in order to avoid stump injuries [13].

2.3.3 - Prosthesis manufacturing

The prosthesis manufacturing process in Portugal, namely in CRPG (Centro de Reabilitação Profissional de Gaia), as in other countries with some minor differences, consists in the following, as stated by Matos, Demétrio [13]:

Initially the level of amputation should be identified to evaluate the state of the residual limb and the viability of using a prosthesis. The stump must be in condition of performing the

connection with the prosthesis through the socket. In some cases, this connection, if not properly made, can lead to a new amputation of the stump.

The socket manufacturing is always personalized because each patient presents different levels of amputation, distinct healing states, different muscular tonus, which leads to an essentially handcrafted production process with low accuracy.

In a first phase of the socket production a dimensional characterization of the residual limb is performed (**Figure 2.8**), analysing the support and articulation zones.



Figure 2.8 - Stump measurement for volumetric reproduction [13].

After, the process of the socket manufacturing starts through the manual production of casts (**Figure 2.9**). Plaster bandages are utilized to reproduce the volume of the residual limb.



Figure 2.9 - (a) Plaster application on the stump, (b) Obtained mold for plaster filling [13].

This negative cast will then be filled with plaster to obtain a replica of the stump (**Figure 2.10**). At this stage, it is also applied a tube inside the solution in order to obtain a support for handle with greater commodity the plaster piece.

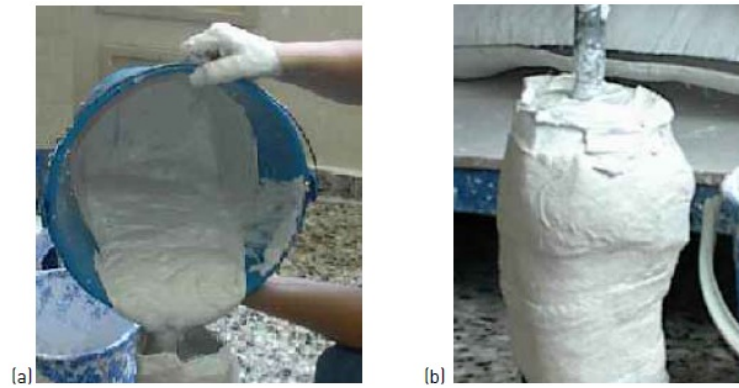


Figure 2.10 - (a) Mold filling, (b) Stump plaster replica obtained [13].

The obtained surface requires a geometrical rectification (Figure 2.11) based on the previously taken measurements of the stump, thus obtaining, manually, the physical support to start objectively the socket manufacturing (Figure 2.12).



Figure 2.11 - (a) Dimensional verification of the stump replica [13].



Figure 2.12 - Final result after adjustments [13].

The stump replica produced will serve as support to produce the prototype of the socket in polypropylene (PP). The entire process happens in the same workshop allowing some autonomy of fabrication in this stage of the prosthesis implementation. The production of the socket in a thermoplastic polymer, as the polypropylene (Figure 2.13), allows a transparency

that reveals itself as indispensable in the moment of evaluating the contact zone during the socket fitting test with the patient.



Figure 2.13 - Socket prototype in polypropylene [13].

Once the socket prototype is concluded, the patient returns to its rehabilitation centre to perform new tests with the purpose of optimizing the contact surfaces. The stump must be perfectly supported to avoid problems that will be reflected during the walk, in the wellbeing of the patient and in the adaptation to the prosthesis.

At this stage the technician benefits from the transparency to analyse and mark the socket to eventually proceed with some modifications (Figure 2.14). The patient will execute its first interaction with the socket and describes its impressions, being this the main methodology to analyse the contact surfaces.

Excessive pressure zones should be eliminated, as well as air pockets, which can cause socket instability. The pressure performed in the ischium by the socket edges it is equally a concern for the technicians, because the termination geometry of the socket can hurt the thigh and cause great discomfort.

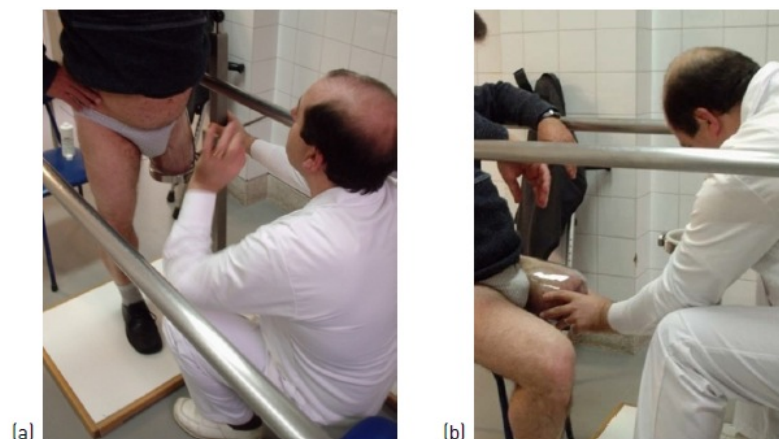


Figure 2.14 - (a) First test of the socket by the patient, (b) Verification of the contact zone [13].

The next step progresses to the production of the final socket having as base the prototype previously produced and tested with the patient. Generally, thermosetting polymeric materials are used to coat the obtained element (Figure 2.15).



Figure 2.15 - Finishing the final socket with a termoplastic material [13].

In contrast with the other components, that are produced industrially, the socket is the only component that can be personalized for the patient. The utilized components to complete the prosthesis are acquired in multiple suppliers accordingly to the needs of each case. The diversity of technical solutions is very extensive and allows to respond to the specificity of the patients having as main restrictions the monetary questions, that pose in most of the cases the major constraints in the production of the final device.

After the delivery of the device to the patient the process of adjustment continues for undetermined time. Every time that adjustment is necessary it should be repeated, and the hypothesis of repeating the socket fabrication subsists. This scenario can be caused by weight variations of the patient due to the use of the prosthesis or/and the sedentary lifestyle caused by the new obstacles that the new mobility imposes. These situations often cause in the elderly patients a demotivation in relation to the use of the device and as consequence a reduced use of the same. The repetition of the process implies outlay of time, human resources and makes it more expensive than the desired.

2.3.4 - Stump-Socket fitting

The stump is considered a new limb responsible for the control of the prosthesis during the walk. To ease this control, it should present some desirable characteristics, such as: proper amputation level, good state of the skin, absence of neuromas and bone spurs, good arterial and venous circulation, good healing and absence of prominent edema.

One of the restrictions will be to think in the utilization of the prosthesis in daily activities, without conflicting with technical issues. The prosthesis should remain connected

to the stub and aligned to avoid lesions. The alignment is reached in 3 phases: the bench alignment, the static alignment and the dynamic alignment.

The developed product can be simple, but the user and the requirements of the product use are complex.

To consider the adaptation between the socket and the stump different factors should be considered, both from the stump and from the socket. In the stump some important features are the geometrical shape, the hardness of the tissues, the bone position and muscular level.

Accordingly to the level of amputation and the stump characteristics there are several types of sockets (**Figure 2.16**) [15]:

- CAT/CAM (Contoured Adducted Trochanteric-Controlled Alignment Method) - socket for transfemoral amputation of ischial contention and full contact. Helps to avoid edema, improves venous circulation and provides better sensitive perception;
- QUAD (Quadrilateral) - socket for transfemoral amputation of rectangular shape on its proximal part. The most important for the force distribution inside the socket;
- PTB (Patellar Tendon Bearing) - socket for transtibial amputation, of support in the patellar tendon, which together with the popliteal dug is used to support the body weight;
- TSB (Total Surface Bearing) - socket for transtibial amputation of full contact, with minimum pressure applied to the residual limb;
- Hybrid models - combination of two different socket types.

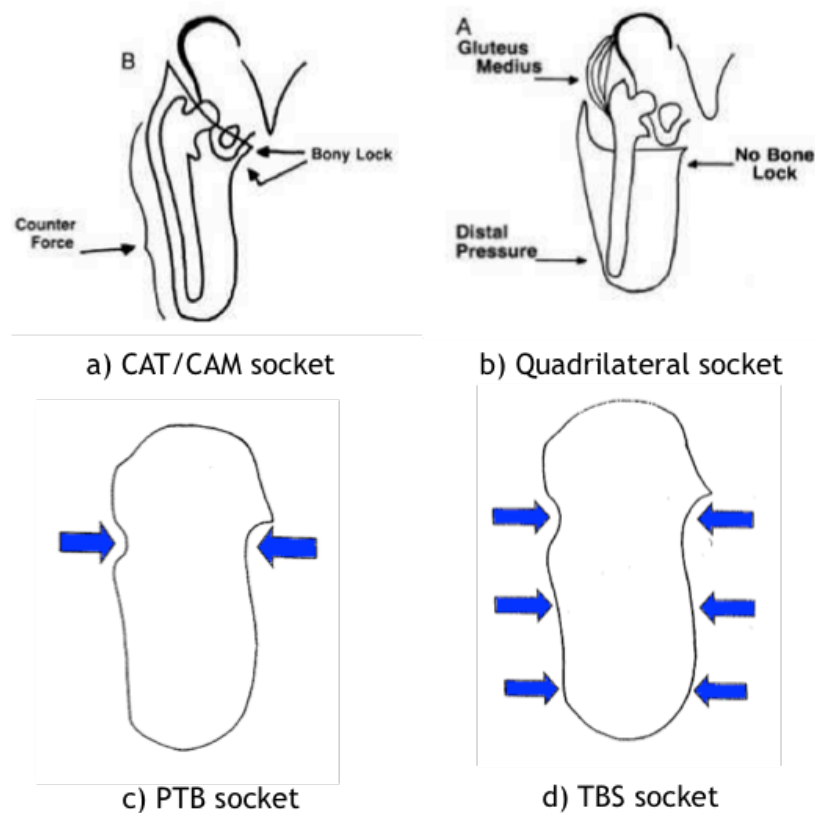


Figure 2.16 - Different types of sockets.

2.4 - Summary

In this chapter, the global constitution of the inferior limb was explained, as well as the types of amputation and its causes. The doctor performing the surgery, depending on the patient, the cause of the amputation and other medical implications, defines the amputation level. After the surgery different stages of the prosthesis use should be followed, however this is not always possible, and some phases are ignored. There are several types of prostheses and components used in its manufacturing, which decision to be used depend on the surgery result and the available budget to the prosthesis production. The adaptation level accomplished will depend both from the stump features and the socket properties, and the patient should be followed by the specialists in order to keep it in the best possible level.

Chapter 3

3D Modelling - methodologies and applications

This chapter divides and describes the existent methodologies to perform 3D measurements and 3D reconstructions along with the 3D modelling techniques applied to the production of prostheses.

3.1 - 3D Measurements

There are several methods to perform 3D measurements and shape acquisition that can be divided in two major groups: contact and non-contact, as it is possible to see in **Figure 3.1**.

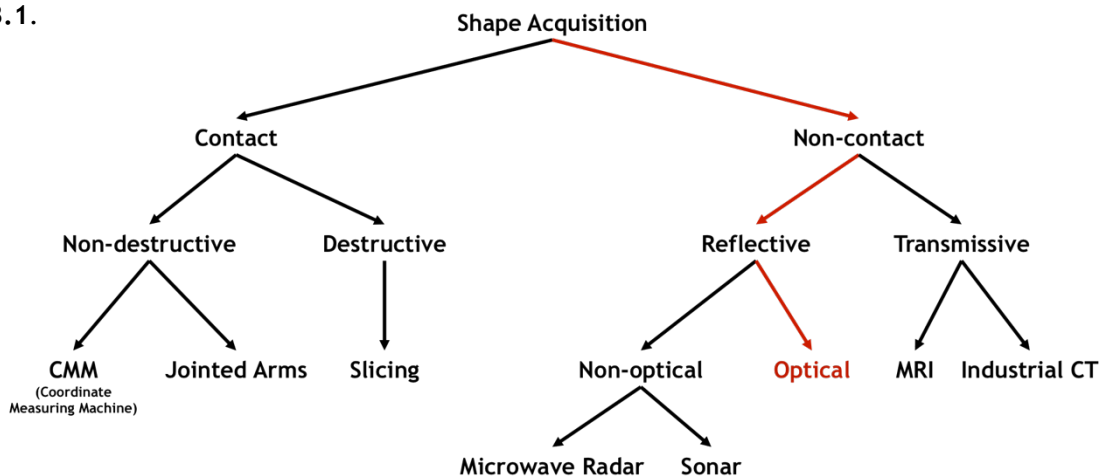


Figure 3.1 - Organization tree of 3D measurement methods for shape acquisition.

Contact methods have significant disadvantages: the working surfaces wear rapidly, the efficiency is low and there is a high risk of inspected surface damage [16], so these are not considered as a possibility. Non-contact methods can be divided in Reflective and

Transmissive, but Transmissive methods are complex and involve great costs, because they are designed for medical applications with the need for high-resolution images both from inner and outer tissues of human body. As in this work the creation of a simpler and low-cost approach is proposed, these methods will not be analysed so thoroughly. So, following the Reflective methods, these can be divided into Non-optical and Optical techniques. The Non-optical methods are highly sensitive to interferences and insensitive at short range, opposing to what is needed in the proposed application. Due to the aforementioned, the exploited methods will belong to the Optical group (Figure 3.2), and will be explained individually.

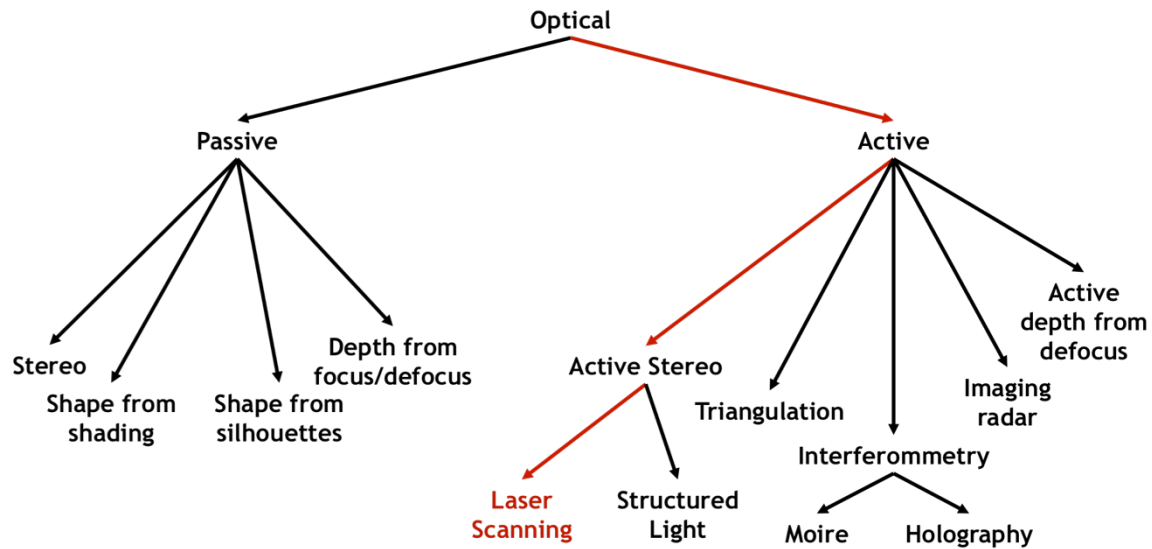


Figure 3.2 - Organization tree of optical methods used for 3D measurements.

The Optical techniques can be divided into two main groups: Passive and Active methods.

3.1.1 - Passive Methods

In passive methods, the scene is first imaged by cameras from two or more points of view and correspondences between images are established. The cameras have to be previously calibrated. The main problem experienced when using this approach is the sparse reconstruction that is obtained since the density is directly related to the texture of the object. This complicates the process of finding correspondences in the presence of textureless surfaces. Therefore, passive reconstruction is rather limited to reconstruct dense 3D surfaces [17].

Images from multiple cameras or successive images from one camera are used, and the shape may be determined by triangulation or the relative shape may be determined from shadows or textures in one image. These methods suffer from problems of the calculation time required in determining the corresponding points between images and of false detection, and in addition it is sometimes limited to relative shape acquisition [18].

3.1.1.1 - Stereo

Algorithms which exploit the differences between two or more pictures of a scene are called “stereo-matching algorithms” [19].

In stereo methods, 3D reconstruction is accomplished in two main steps, the first addressing the matching problem and the second addressing the reconstruction problem. The first recognizes if two or more points belonging to different images are the projection of the same point P of the 3D scene. The second uses these correspondences in order to estimate the exact position of P in the 3D space [20].

3.1.1.2- Shape from shading

The shape from shading algorithms gets the surface shape from the brightness of a single picture. It relies on approximations of the reflectance characteristics of the object to be reconstructed, that are the relationships between incoming illumination to a point on the surface and the light reflected by it [20].

3.1.1.3- Shape from silhouettes

Algorithms, which reconstruct 3D objects using only silhouette information extracted from a set of images, are called “Shape from Silhouette” methods. All these methods must face the problem of extracting silhouette information from the set of images, which means, they must identify the points belonging to the object, separately from those belonging to the background. This problem does not have a general solution as it strongly depends on the scene characteristics [20].

3.1.1.4 - Depth from focus/defocus

There are two techniques to infer depth from a set of defocused images, called “Shape from Focus” (SfF) and “Shape from Defocus” (SfD). The first one, SfF, acquires a large number of images with small focal settings differences. The second one, SfD, needs only few differently focused images, typically two or three, in order to estimate depth information. In both cases, defocused images are obtained by varying settings like the lens focal length, the aperture radius or the distance between the object to be acquired and the camera (**Figure 3.3**). Afterwards, depth is estimated by comparing the blurriness of different regions in the acquired images [20].

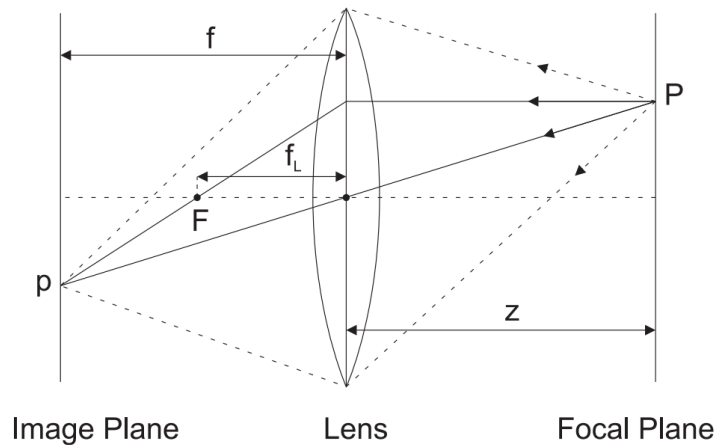


Figure 3.3 - Image formation with lenses: all the light rays coming from a point P in the focal plane are projected into a single point p in the image plane [20].

3.1.2 - Active Methods

Active methods are techniques that use laser or other forms of radiation for shape determination using the radiation angle of the light source and the position on the image. In this type of methods a high accuracy result can be obtained without complicated calculation processes, however the measurement time depends on the specificities of the method [18].

3.1.2.1 - Active Stereo

Laser Scanning

A laser scanning system is characterized by a simple principle of operation, in which a laser plane is projected perpendicularly to the surface to be measured. The intersection of the projected plane with the surface under inspection becomes evident in a form of a line that assumes the contour of the surface thus allowing the extraction of tridimensional information to be performed [21].

Laser scanning systems have high resolution but present some limitations, as the high scanning time when generating high volume of information and the occlusions that may occur due to the shapes of the surfaces being scanned. For higher resolutions the cost increases, due to the need for more powerful sources of light, more sensitive optical sensors and more precise positioning components [22].

The great advantage of laser scanning methods is that there is no ambiguity in identifying features in the images [23].

Structured Light

Structured light projection systems can be used in a wide range of applications where information about shape or its deviation is required. It is a fast, contactless and relatively cheap method [24]. These techniques are based in the projection of a pattern of light and the visualization of the illuminated scene from one or more points. As the used patterns are codified, it is possible to easily establish correspondences between the points of the image and the projected points. Recurring to triangulation, 3D information can be obtained [22].

The Structured light approaches for inspecting internal surfaces might be divided into 3 categories, according to sensor types [25]:

- Single-point: a sensor inspects the internal surface point by point. The inspection takes a long time;
- Single-line: a sensor inspects a sectional contour of the internal surface at one time. It fits for inspecting a big space rather than a small space since this kind of sensors are often big;
- Multi-line: a sensor inspects the internal surface by multi-lines distributed on a 3D surface.

A projected line produces a unique set of coordinates in the camera, but multiple lines, or a projected grid, produce multiple sets. One of the most difficult issues in structured light approaches is the identification of each projected feature. The more lines are used the greater is the confusion caused. There are several methods to solve this sorting problem, such as the Moiré topography [23].

Coded structured light techniques can overtake these problems. This technique is based on the projection of a single or a set of patterns onto the measuring scene, which is then viewed, by a single camera or a set of cameras. The patterns are specially designed so that codewords are assigned to a set of pixels. Every coded pixel has its own codeword, so there is a direct mapping from the codewords to the corresponding coordinates of the pixel in the pattern [26].

Specular reflection from polished surfaces can complicate reliable measurement of reflected light, but in applications in which imaging of human body structures is involved the surface to be measured reflects diffusely, so structured light illumination is a good technique [23]. It also presents a problem related to the ambient light. The projected light must be much brighter than the ambient light, which is not possible or convenient in all the application scenarios [23].

3.1.2.2- Triangulation

The triangulation is a process that allows the 3D point position to be calculated from two images in which that point is visible. This process requires the intersection of two known lines in the space. In the presence of noise intersection this may not occur, becoming necessary to estimate the best approximation [27].

3.1.2.3- Interferometry

Interferometry methods operate by projecting a spatially or temporally varying periodic laser pattern onto a surface, followed by mixing the reflected light with a reference pattern. The resulting interference signal is then demodulated to reveal the variation in surface geometry. The measurement resolution is very high, since it is a fraction of the wavelength of the laser radiation, and that is why it is mostly used in surface quality control and microprofilometry [28].

3.1.2.4- Imaging radar

Imaging radar methods are based in signal propagation, where three main variables are considered: the distance to the object (determined in function of the next two), the speed of signal propagation, and the time that the signal takes from the radar transmitter to the object and back to the radar receiver. In some types of imaging radars there are some unknown scene parameters at the reflecting point that must be considered, such as the distance and the surface reflection coefficient [29].

3.1.2.5- Active depth from defocus

The goal is to estimate the focus error (and hence depth) in each image region from two or more images obtained for different values of the aperture, a , or focal plane position, d_i . Estimation of focus error requires a model of the optical system. The most common model is based upon geometric optics; the point spread function of the defocus process is represented by the blurring of an ideal point source where the intensity of the point source is spread uniformly over a circular extent varying in radius with the amount of defocus - a blur circle [30]. However this presents a problem that is the amount of defocus depends on the presence of texture [31].

3.2 - 3D Reconstruction and Modelling

Surface reconstruction is a difficult problem, because measured points are usually unorganized and noisy, the surface can be arbitrary, with unknown topological type and sharp features. A good sampling should be dense in detailed area and sparse in featureless parts [3].

3.2.1 - Classification of the reconstruction algorithms

It is very complicated to classify all the reconstruction methods, because the universe of algorithms is quite large [3], however this classification can be performed according to different characteristics.

Classification according to the quality (type) of the input data [3]:

- Unorganized point clouds: algorithms working on unorganized data have no other information on the input data except their spatial position. They do not use any assumption on the object geometry and therefore, before generating a polygonal surface, they usually structure the points according to their coherence. They need a good distribution of the input data and if the points are not uniformly distributed they easily fail;
- Structured point clouds: algorithms based on structured data can take into account additional information of the points (e.g. breaklines).

Classification according to their spatial subdivision [3]:

- Surface oriented algorithms do not distinguish between open and closed surfaces [32];
- Volume oriented algorithms work in particular with closed surfaces and generally are based on the Delaunay tetrahedrization of the given set of sample points [33-35].

Classification based on the type of representation of the surface [3]:

- Parametric representation: these methods represent the surface as a number of parametric surface patches, described by parametric equations. Multiple patches may then be pieced together to form a continuous surface. Examples of parametric representations include B-spline, Bezier curves, and Coons patches [36];
- Implicit representation: these methods try to find a smooth function that passes through all positions where the implicit function evaluates some specified value [37];
- Simplicial representation: in this representation the surface is a collection of simple entities including points, edges and triangles [3].

According to the mean of representation, approximated or interpolated surfaces can be generated [3]:

- Approximated surfaces do not always contain all the original points, but points as near as possible to them. They can use a distance function (shortest distance of a point in space to the generated surface) to estimate the correct mesh [32]. In this group we can also insert the warping-based surface reconstruction (they deform an initial surface so that it gives a good approximation of the given set of points) [38] and the implicit surface fitting algorithms (they fit, for example, piecewise polynomial functions to the given set of points) [39];

- Interpolated surfaces are instead used when precise models are requested: all the input data are used and a correct connection of them is necessary [40].

Classification according to the different assumptions of the algorithm [3]:

- Algorithms assuming fixed topological type: they usually assume that the topology of the surface is known *a priori* [41, 42];

- Algorithms exploiting structure or orientation information: many surface reconstruction algorithms exploit the structure of the data for the surface reconstruction. For example, in the case of multiple scans, they can use the adjacency relationship of the data within each range image [43].

3.2.2 - From points to surfaces

The conversion of the measured data into a consistent polygonal surface is generally based on four steps [3]:

1. pre-processing: in this phase erroneous data are eliminated or points are sampled to reduce the computation time;
2. determination of the global topology of the object's surface: the neighbourhood relations between adjacent parts of the surface has to be derived. This operation typically needs some global sorting step and the consideration of possible 'constraints' (for example breaklines), mainly to preserve special features (like edges);
3. generation of the polygonal surface: triangular (or tetrahedral) meshes are created satisfying certain quality requirements;
4. post-processing: when the model is created, editing operations are commonly applied to refine and perfect the polygonal surface.

3.2.3 - Pre-processing operations

Editing operations on the measured points are very important before generating a polygonal surface. The pre-processing operations usually are [3]:

- data sampling based on the curvature of the points or uniformly applied. In the case of scanner data, this step (down-sampling) is mandatory in order to reduce the input redundancy and to remove a certain amount of errors introduced by the limitations of the scanning device [44].

- noise reduction and outliers rejection: statistical methods are applied taking into consideration the surface curvature and trying to preserve the measured features. In the case of image matching results, wrong correspondences can be removed automatically [45, 46] or manually with visual inspection.

- holes filling: gaps in the point clouds are closed adding (manually or automatically) new points and using the curvature and density of the surrounding points.

3.2.4 - Triangulation and mesh generation

A triangulation converts the given set of points into a consistent polygonal model (mesh). This operation partitions the input data into simplices and usually generates vertices, edges and faces (representing the analysed surface) that meet only at shared edges. Finite element methods are applied in the discretized measured domains by dividing it into many small 'elements', typically triangles or quadrilaterals in two dimensions and tetrahedral in three dimensions. An optimal triangulation is defined measuring angles, edge lengths, height or area of the elements while the error of the finite element approximations is usually related to the minimum angle of the elements [3]. The vertices of the triangulation can be exactly the input points or extra points, called Steiner points, which are inserted to create a more optimal mesh [47]. Triangulation can be performed in 2D or in 3D, according to the geometry of the input data [3].

3.2.5 - Post-processing operations

The created polygons usually need some refinements to correct imperfections or errors in the surface [3]:

- edges correction: faces can be divided in two parts, moved to another location or contracted;

- triangles insertion: holes can be filled constructing polygonal structures that respect the surrounding area, and incomplete meshes can also be repaired [35, 48];

- polygons editing: the number of polygons can be reduced preserving the shape of the object or fixing the boundary points. The polygonal model can also be improved adding new vertices and adjusting the coordinates of existing vertices, and spikes can be removed with smooth functions.

3.3 - Prosthesis 3D Modelling

Traditionally, the design of the prosthetic socket relies on the observations, skills and experiences of individual prosthetists. As a result, conventional socket designs are largely subjective and vary among prosthetists [49].

In recent years, a great number of methods to perform the 3D modelling of the residual limb have been developed, but only a few for the inner surface of the prosthesis socket.

Some of the methods applied to obtain the internal model of the socket are contact methods, such as, the use of a pivoting arm. During the measurement with this system, the socket is rotated around a longitudinal axis as a measuring arm tip touches the inside of the socket, and the socket moves along this axis [49]. The contact methods are used in some CAD/CAM socket design systems [50, 51].

When designing the socket, the most common procedure is to use the 3D modelling of the residual limb, and from that get to the ideal design of the socket.







To obtain the 3D model of the residual limb there are several techniques, using some technologies existent in the hospitals [49]:

- CT: using computer tomography it is possible to reconstruct the 3D shape of the residual limb from a number of 2D slices taken transversely to the limb's long axis. This same technique can be used to reconstruct the 3D model of the prosthesis socket.

- MRI: Magnetic resonance imaging could be used to establish computational models of residual limbs. MRI could provide high resolution and clear differentiation between tissues. However, it is expensive and requires long scanning time.

On the market it is possible to find multiple CAD/CAM systems, as it is possible to see in **Table I**.

Table I: Prosthetic CAD/CAM systems available in the market (AK=Above Knee, BK=Below knee) [8]

Company	System		Price
	Acquisition Technologies	Laser scanner with 2 cameras, a miniature transmitter for the body and scan-through-glass technology, or manual measurements	Non available
	Acquired Data	External shape of AK and BK residual limb	
	Stump/Socket Modelling	AK: starting from a library of templates -> external shape of the socket AK/BK: using oblique, transverse and circumferential measurements -> automatic generation of the check socket	
	Acquisition Technologies	Laser reflection scanner with 1 or 2 cameras	Non available
	Acquired Data	External shape ok AK and BK residual limb	
	Stump/Socket Modelling	BK: proximal brim and shape utilities help to transform areas anywhere on the acquired shape -> external shape of the socket AK: standard shapes from library, tools to change volume, length, circumferences -> model of the socket	
	Acquisition Technologies	Structured light projection, digital camera or manual measurements	Non available
	Acquired Data	External shape of AK and BK residual limb	
	Stump/Socket Modelling	BK: on the geometry of the residual limb in defined areas you can apply compression or create build-up areas -> external shape of the socket AK: the desired shape is created using a protocol based on manual measurements -> positive model of the socket	
	Acquisition Technologies	Digital camera or manual measurements	Non available
	Acquired Data	External shape of AK and BK residual limb	
	Stump/Socket Modelling	BK: calculate circumferences and volume of the stump and allows to modify the acquired shape -> positive model of the socket AK: measurement taken from the residual limb -> model of the check socket	
	Acquisition Technologies	Laser scan with 1 camera	15990€
	Acquired Data	External shape of AK and BK residual limb	
	Stump/Socket Modelling	AK/BK: starting from a shapes library, adding check measurements, checking volume and circumferences -> positive model of the socket	
	Acquisition Technologies	High quality LED projector (structured light) and single camera (digital)	Spectra™ Scanner - 11800€
	Acquired Data	External shape of AK and BK residual limb	
	Stump/Socket Modelling	AK/BK: automatic 3-dimensional measures recurring to as many landmarks as required, adjustment with Canfit™ design software	

3.4 - Summary

There is no simple way of determining which method best suits any particular application, and in general, the decision is based upon a combination of the following factors [52], namely: inspection speed; equipment size constraints; ease of construction, installation, operation and maintenance; operational flexibility; expense; mechanical robustness and defect resolution capabilities.

The chosen method was laser scanning as it presents a good inspection speed, it can be adapted to the size constraints of the socket, it is relatively easy to build, it is less expensive than the other possible methodologies, and its resolution can be adapted by varying the camera used.

Chapter 4

Laser Scanning System

In this chapter, the planning to create a new laser scanning system, using a circular laser line, for 3D modelling of a socket inner surface will be presented, as well as the description of the same. The experimental procedure that was followed to acquire the results and the developed user interface are also explained.

4.1 - System Design and Implementation

To perform the 3D measurement of the inner surface of the socket, it was decided to project a laser light plane in a direction perpendicular to that of the longer axis of the socket. From this projection results an approximately circular line, since the geometrical form of the socket is approximately cylindrical. The envisaged setup also makes use of a camera whose image plane is parallel to the projected laser plane. The camera field of view is centred with the longer axis of the socket and, consequently, with the centre of the laser circle. To produce the laser plane, a laser beam is directed into the vertex of a conic mirror. In order to obtain the complete 3D measurements, there is the need to scan along the z axis (**Figure 4.1**). This was accomplished with the use of a step motor and a mechanical system that we have designed. Special care was placed in the design, fabrication and assembly of the scanning system in order to ensure its alignment was maintained during operation, thus avoiding the introduction of errors into the measurements.

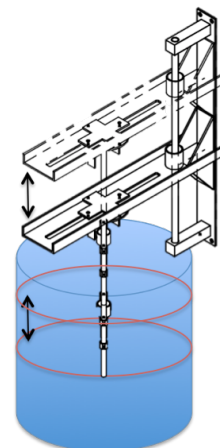


Figure 4.1 - Scheme depicting the laser scanning principle along the z-axis.

By computing the distance between each pixel of the laser line, and the centre of the circle, it is possible to obtain the position of each point of the circular line. After the system calibration (to infer the real position of the points), by joining the information resulting from the analysis of all the images acquired along the z axis it is possible to reconstruct the 3D model of the inner surface of the socket (**Figure 4.2**).

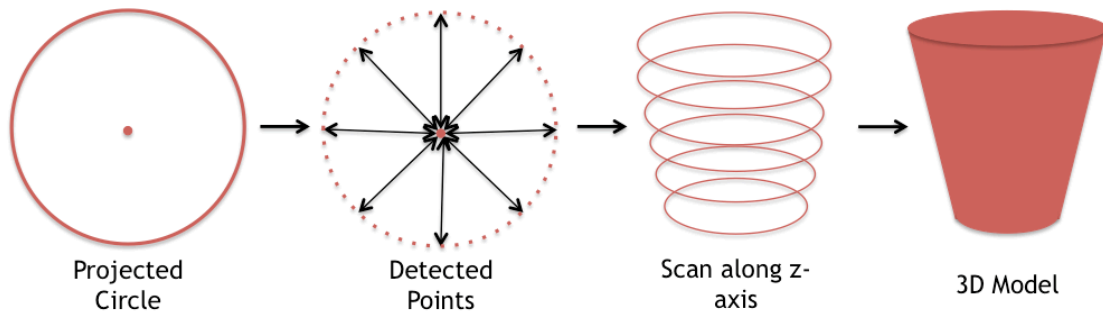


Figure 4.2 - Principle of sample analysis and model reconstruction.

The mechanical system (technical drawings in appendix I) that was designed and implemented to perform the movement of the system along the z-axis is shown in **Figure 4.3**.

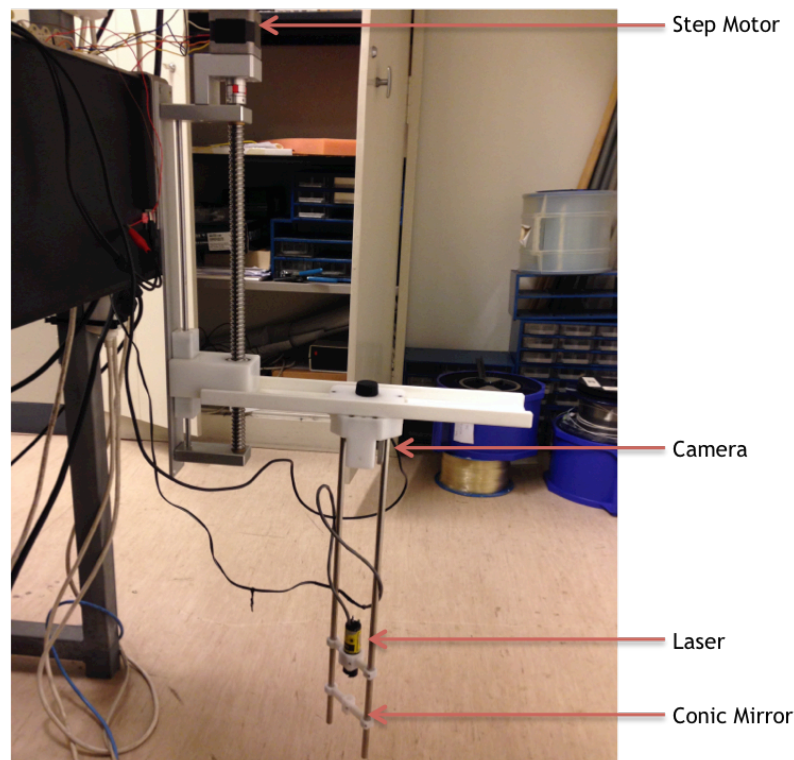


Figure 4.3 - Main components of the developed scanning system.

In the photo of **Figure 4.3** the main components of the system can be seen, namely a Step-Syn Sanyo Denki Stepping Motor; a Microsoft® LifeCam VX-800 camera; a laser; and a conic mirror.

The movement along the z axis is accomplished with the step motor which is linked to a ball screw. The rotation of the motor, causes the ball screw to rotate which forces the nut, and consequently the system, to move up and down according to the rotation direction of the screw (**Figure 4.4**).

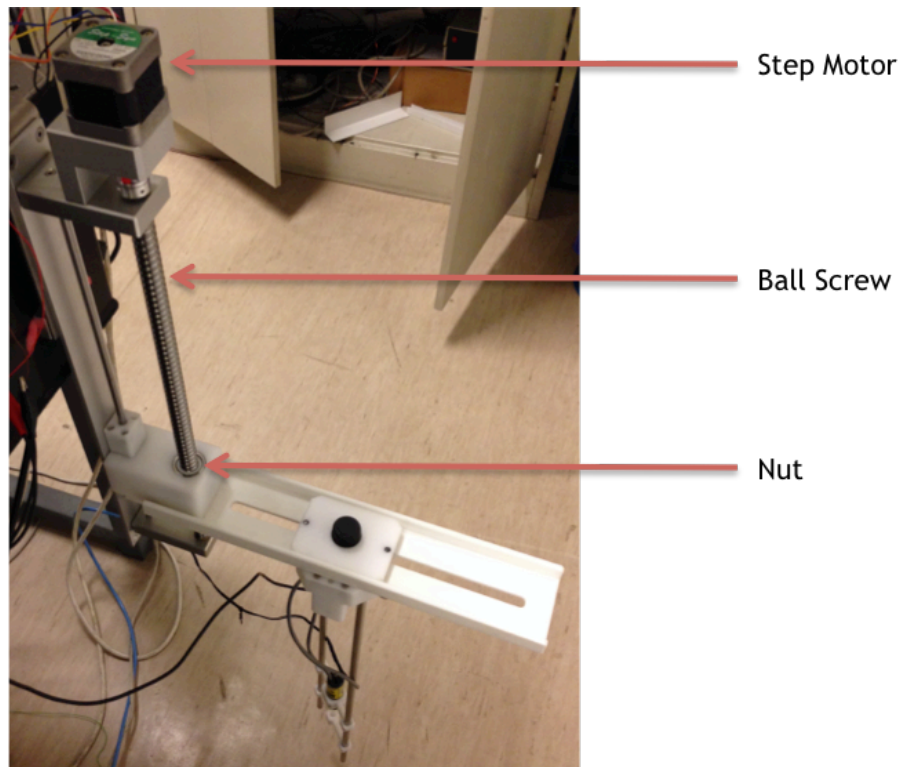


Figure 4.4 - Main components of the developed mechanical system that enable it to perform the movement along the z axis.

The presence of guides to fixate the laser and to align the conic mirror occluded part of the light projected into the object. To solve this issue, the system enabled the rotation of the guides, and consequently of the laser and the mirror, but not of the camera, thus changing the position of the occlusion of light in the object, during the second scan that was performed in the opposite direction. The scanning in two directions (down and up) simultaneously solved the problem posed by the occlusion of information in the object (caused by fixation guides) and allowed more measurements to be performed, which can be further used for accuracy improvement.

As it is possible to see, the produced solution solves every problem and need of the problem at hands: it has the appropriate size to move inside the socket, it keeps the system fully aligned and it allows adjustments to be made in accordance with the socket being analysed.

The second step was to design and set up an electronic circuit to allow the control of a step motor with a computer, in order to move the system up and down during the scanning, with a speed that could be either set by default or defined by the user. For that the circuit in appendix II was developed.

The circuit to control the step motor has two main parts: an Arduino Uno microcontroller to communicate with the PC; and an electronic circuit to supply voltage and current to the step motor, composed by TIP33C and BC337 transistors, diodes and resistors.

Table II lists the main components of the laser scanning system and the respective specifications.

Table II: Specifications of the laser scanning system components

Component	Specifications
Microsoft® LifeCam VX-800 Webcam	Sensor: CMOS VGA sensor technology Resolution: 0.31 megapixel (640 x 480 pixels) Field of view: 59° diagonal field of view Imaging Features: Fixed focus; Automatic image adjustment with manual override
Lasiris Red Laser	Single Point Wavelength: 660 nm Emitting power: <1mW
Ball Screw SN 12x5Rx2 T5 400	Course: 400mm Step: 5mm Nominal diameter: 12mm
Edmund Optics Conic Mirror	Cone Lens Aluminum Coated 3mm diameter 3 mm length (4.5 mm total) 90° reflection ±6 arcminutes angle tolerance
Step-Syn Sanyo Denki 103H548-0440 Stepping Motor	One Axis 6-wire Basic Step Angle: 1.8° Voltage: 3.6 V (Overloaded supply at 6.5 V) Current: 1.2 A/Phase Holding Torque: 0.265 N.m Mass: 0.28 Kg Allowable radial load: 28N Allowable thrust load: 10N
Arduino UNO	ATMEGA 32 w/ USB

	Power Supply: 5 V
Topward 3303 DC Power Supply	Voltage: 0-30 V Current: 0-3 A

The main components characteristics can be found in **Table III**.

Table III: System specifications

Illumination	No direct lighting
Scanning Course	0-260 mm
System step	0.1-260 mm
Power Supply	6.5 V
Current	2-3 A
Scanning diameter	85 - 230 mm

4.2 - Experimental Procedure

In order to remain consistent and to be able to compare all the results obtained and analysed, a procedure to acquire images was defined and followed in every test performed during the realization of this work.

The first step consisted in placing the system in its highest position, in order to be able to place the object of study under the system (**Figure 4.5**). Then lower the system until the conic mirror support at the same level as the top of the object, and center the object with the system.

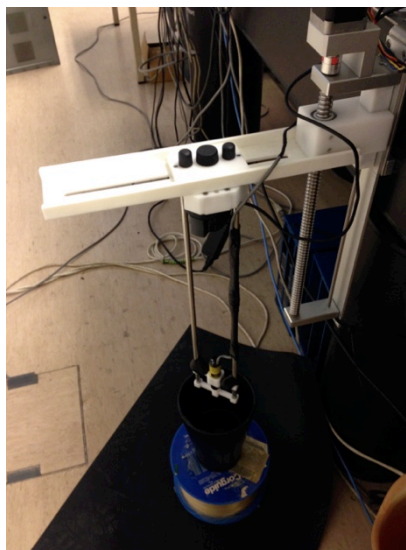


Figure 4.5 - System in the highest position.

To center the object with the system, two different methodologies were followed, depending of the type of object in study. For objects with regular and constant shape (a cone or a cylinder, for instance) several measurements were performed to assure that the system was aligned with the center of the object, as demonstrated in the figure below (**Figure 4.6**).

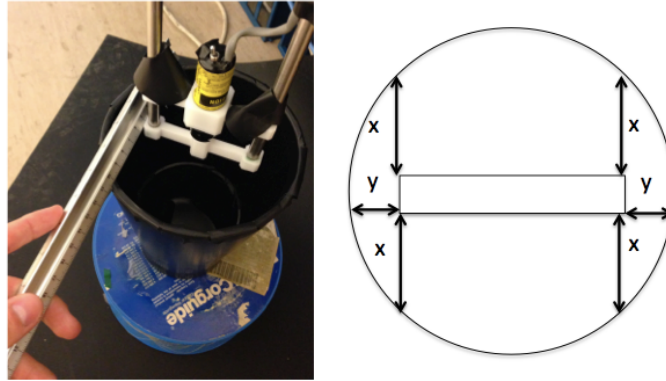


Figure 4.6 - Alignment of the object with the system.

When working with objects of irregular shape, it is difficult to identify the geometrical center of the object, and the positioning of the object will affect the results and the performance of the system. However, the system works and presents good results, regardless of the position of the object of study, since this is not blocking the movement of the system.

The object of interest of this thesis (the lower limb prosthesis socket) is an object with an unknown shape but with some features that allow the alignment. The conic mirror was removed from the system thus allowing the laser beam to be used as a reference to place the object. In the specific case of the socket, it has an opening in the bottom that can be aligned with the laser point (**Figure 4.7**). When using the developed system, the most important was to have all the acquired images centered in the same point, so the collected points that would posteriorly form the 3D model would all have the same reference, that could then be manipulated in order to make it correspond to the real axis correspond to the real axis of the socket and the amputee residual limb. After everything was aligned, the conic mirror was placed again in its marked position.

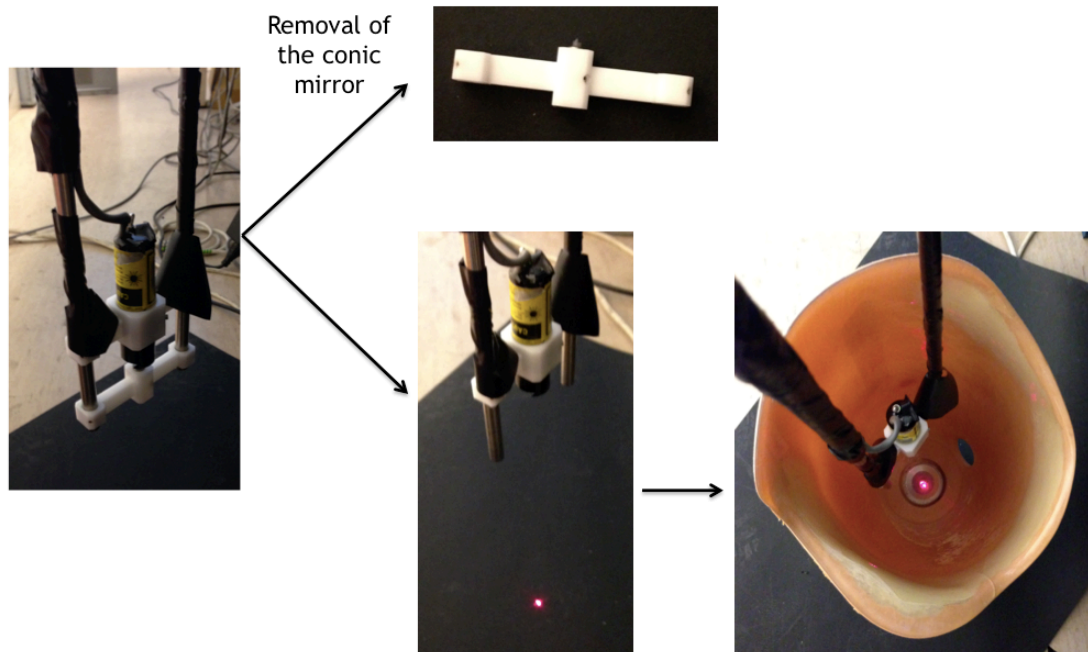


Figure 4.7 - Alignment of the prosthesis socket with the system.

The next step was to determine the length (along the z axis) of the scanning to perform, place the system in the position desired to begin the process and turn on the laser. Finally run the software with the information of the length of the scanning, and the step (z distance) between consecutive images. The system stopped when the scan length defined by the user was reached. Afterwards, a message asking to rotate system was displayed, which then allowed a second scan to be performed in the opposite direction (**Figure 4.8**).

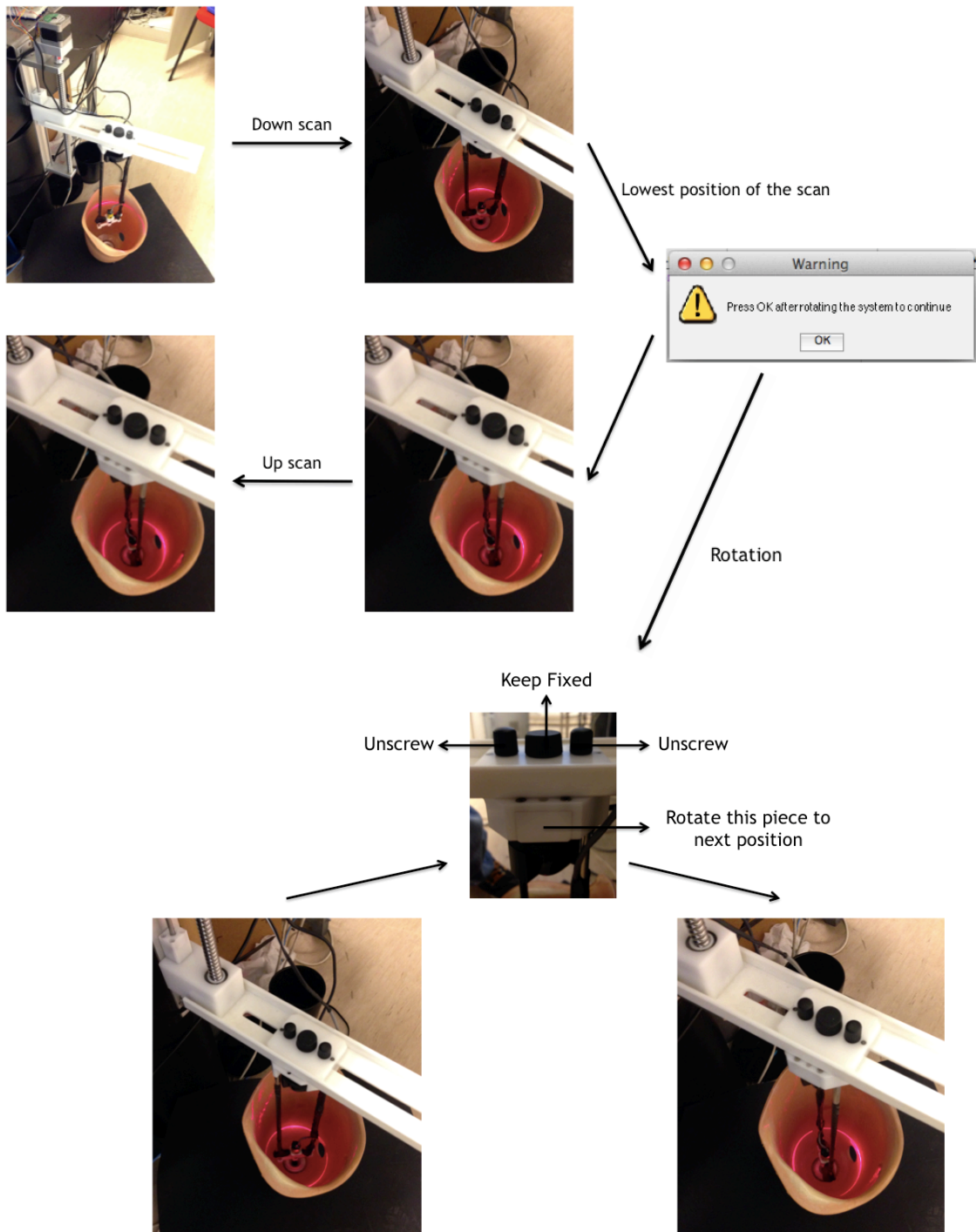


Figure 4.8 - Complete scanning (two directions with rotation).

4.3 - User Interface

During this work a user interface was developed to allow different users to easily manipulate the system, and analyse the acquired scan images. The interface was thought to be user friendly and to allow multiple actions, either working with the system or with previously acquired results.

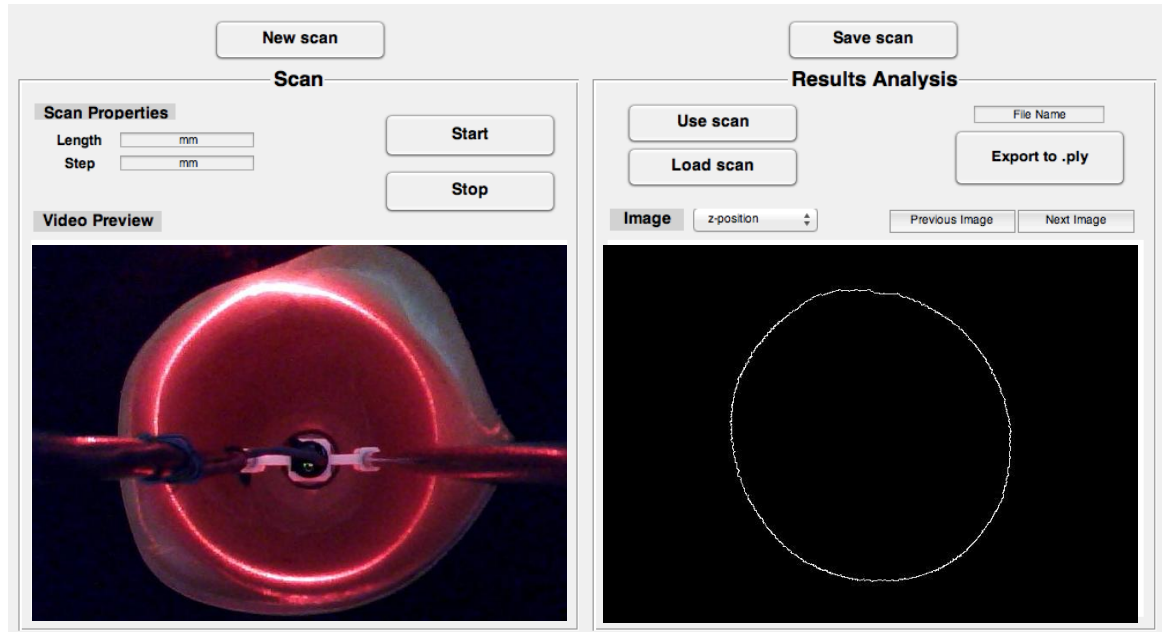


Figure 4.9 - Developed user interface, for system control and result analysis.

As shown in **Figure 4.9** the developed Matlab interface has two main blocks, one for the scanning and for control the system (“Scan”), and other for the analysis of the results of the last performed scan, or previously stored scans (Results Analysis).

To start a scan, the length and the z-step between acquired images should be inserted by the user, and then press the button “Start”. A message will appear with “Scanning...” until the system reaches the length indicated by the user, then the user will be requested to rotate the system and press OK for the system to continue. The message “Scanning...” will appear again until the scan finishes, presenting then the message “Scan complete”. If the user needs to interrupt the scanning, he only needs to press the button “Stop”. To perform a new scan, the button “New scan” can be pressed, and the interface will be set again to default values. In the inferior window of the first block, the view from the system camera is constantly being displayed (“Video Preview”).

After the scan the results can be saved by pressing the button “Save scan” and/or analysed by pressing the button “Use scan”. Results previously acquired from other scans can also be analysed, by pressing the button “Load scan”. When the analysis of the result starts, the message “Analysing...” is displayed, and when it is finished the message “Analysis

complete” appears. The results will be displayed in the inferior window of the second block, allowing the user to navigate between images, either by using the pop-up menu and choosing the z-position associated to the result desired, or by navigating between consecutive images, using the buttons “Previous Image” and “Next Image”. In the end, the user can introduce the file name under which he intends to store the point cloud generated from the analysis of the images acquired during the scanning process, and then press the button “Export to .ply”, to export the file to “.ply” format so that can be imported by 3D mesh processing software, such as MeshLab, for example.

4.4 - Summary

A laser scanning system with the required features for the purposed application was designed and built, using a complete set of components chosen by their specifications.

An experimental procedure was defined in order to keep the coherence between all the acquired results and allow a more accurate analysis of the same.

A user interface was also developed to allow different users to easily use the developed system.

Chapter 5

Image Processing Algorithms for Segmentation of the Circular Laser Line

This chapter exposes the two algorithms that have been implemented to detect and segment the laser line in the images acquired with the system. The results obtained with these two algorithms were analysed and compared to each other. Measurements of the object and Ground Truth references were manually defined by a human expert in order to objectively infer the individual and comparative performance of the two algorithms.

5.1 - Methodology

As previously explained in Chapter 4, the results of the scanning procedure using the implemented system were images in which a highlighted shape of interest with an approximately circular shape was present. Therefore the need to segment this shape arose and in this section the implemented methodology is described.

No specific method of segmentation was found in the state of the art for the intended purpose with good results. As an example, the Snakes [53] that search for active contours were tested, but the need for a starting point to be introduced by the user and the extreme sensitivity to detect contours that do not belong to the shape of interest, showed that this was not a good approach.

With the goal of segmenting the needed shape with good results, two different algorithms were specifically developed: Maximum Intensity with Minimum Path (MIMP) and Gradient Average with Minimum Path (GAMP). Both of the codes pretended to segment the projected laser line by searching its geometrical central points, since this should be the more accurate and consistent approach once the line does not always have the same thickness in all its extension and in all the captured images. Both of them also resort to the minimum path algorithm developed by Oliveira, H. [54]

Initially both algorithms followed the same steps starting with the acquired image (Figure 5.1).

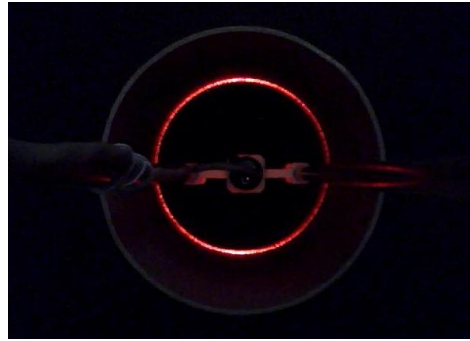


Figure 5.1 - Example of an image acquired by the scanning system (original RGB image).

The acquired image was in RGB format, so to facilitate the segmentation of the circular laser line, only the red component was chosen since the used laser was emitting in the red region of the visible spectrum (Figure 5.2).

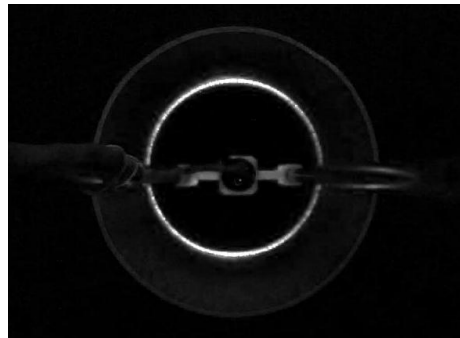


Figure 5.2 - Red component of the previous RGB image.

The center of the circular laser line was automatically detected (Figure 5.3), by detecting the center of the dark circle formed by the back of the laser, that appears in every acquired image, recurring to “imfindcircles”, a Matlab standard function. This tool detects dark circles and devolves the center coordinates and the radius of the detected circles.

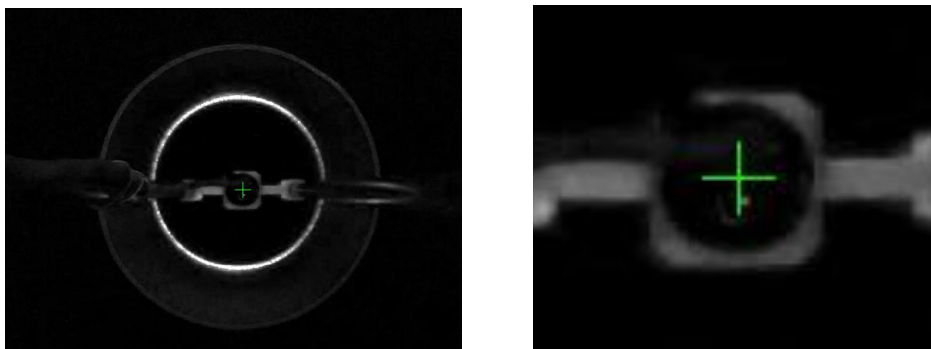


Figure 5.3 - Detected center in the acquired image, with a zoom on the right.

After the center detection and the isolation of the red component an image enhancement routine was applied through the use of a tophat filter with a structural element in form of a disk with a five pixel radius, with the purpose of enhancing the laser line relatively to the background.

The resulting image was then passed from Cartesian coordinates to Polar coordinates (**Figure 5.4**) to simplify the following steps, once in Polar coordinates the object to segment was approximately a straight line instead of the circular shape that was represented in Cartesian coordinates.

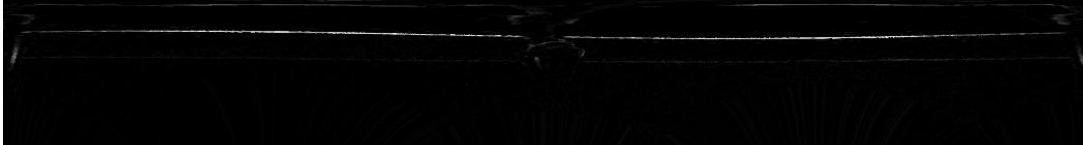


Figure 5.4 - Example of an acquired image by the developed system in polar coordinates.

After this the two developed algorithms followed different paths.

The MIMP algorithm had as main feature the search for the maximum intensity in each column of the polar image, because that corresponded to the geometrical center of the laser line (once it was the brightest object in the acquired image). Each column is scanned from top to bottom and in the opposite direction and for each direction the position of the first maximum found was stored. After, a new polar image is created. In that new image, for each column, if the same maximum was detected in both the top-bottom and the bottom-top search procedures the position of that maximum is assigned with the value of the corresponding detected maximum. In the columns in which the detected maxima were not in the same position, this new image contained the data from the original image (**Figure 5.5**).

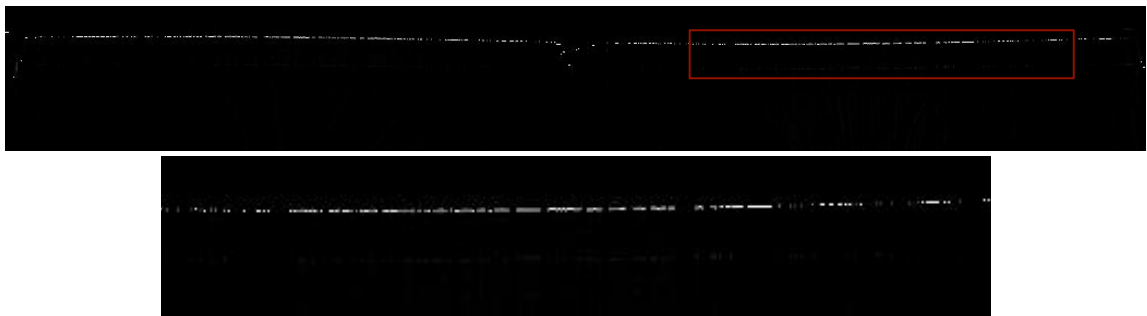


Figure 5.5 - New polar image containing in each column either the detected maximum in the position it was detected or the data from the original image (on the top), with a zoom of the selected area (below).

This analysis of each column of the polar image was in reality performed between the 80th line and the last, because the lines 0 to 80 correspond to the area occupied by the system fixation for the laser (**Figure 5.6**), so there will never exist useful information in that region, thus allowing one to immediately discard it.

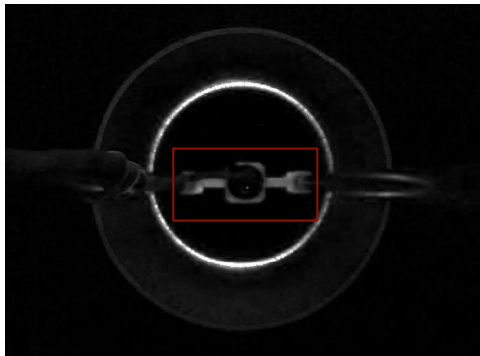


Figure 5.6 - Area of the image discarded from the analysis corresponding to the physical space occupied by the laser support.

The created image was then passed through the minimum path algorithm that finds the minimum path that starts and ends in the same point of the line and passes through the detected maxima, thus resulting in the segmented laser line (**Figure 5.7**).

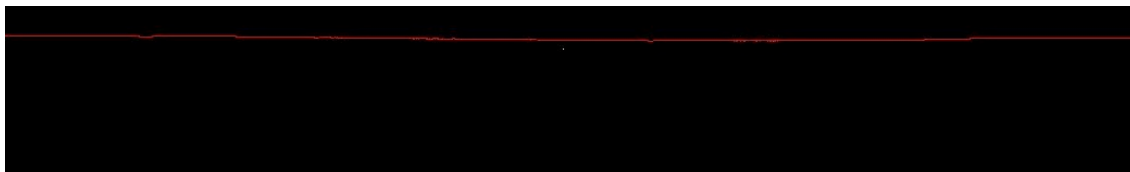


Figure 5.7 - Minimum path resulting from the MIMP algorithm.

The resulting image with the segmented laser line (with 1 pixel width) was then converted again to Cartesian coordinates and the (x,y) position of each point of the line relative to the detected center was extracted (**Figure 5.8**).

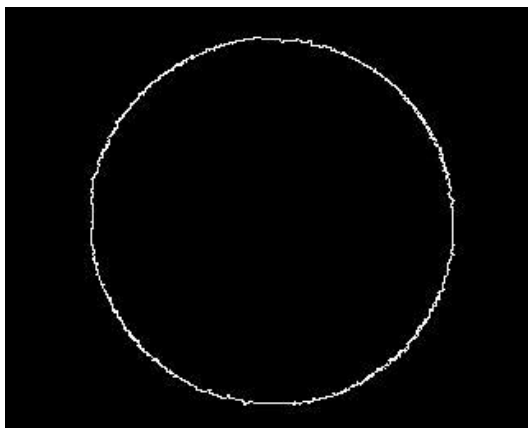


Figure 5.8 - Segmented circular laser line resulting from the MIMP algorithm.

As for the GAMP algorithm, the main feature was the search for the inner and the outer limit of the laser line, followed by an average of both, as it was perceived this could be a good indication of the geometrical center of the laser line. The positive (**Figure 5.9**) and

negative (Figure 5.10) gradients of the previously processed polar image were found [55], resulting in two different new polar images.

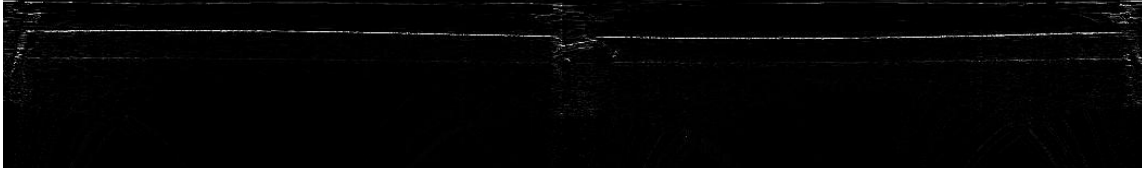


Figure 5.9 - Positive gradient image resulting from the original polar image.

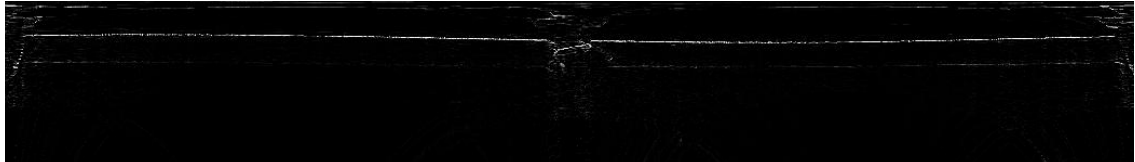


Figure 5.10 - Negative gradient image resulting from the original polar image.

As in the MIMP algorithm, the gradient images were then analysed column by column from the top to the bottom, and from the bottom to the top, storing the maxima detected in the same position in both searches. Next, a new polar image was created with the mean of the maximum position in the same column of both gradient images, if in the same column of both gradient images a maximum was detected, and with the data from the original image in the cases where the same was not verified (see Figure 5.11). As in the MIMP algorithm, in this one the analysis was also performed from the line 80 to the last.

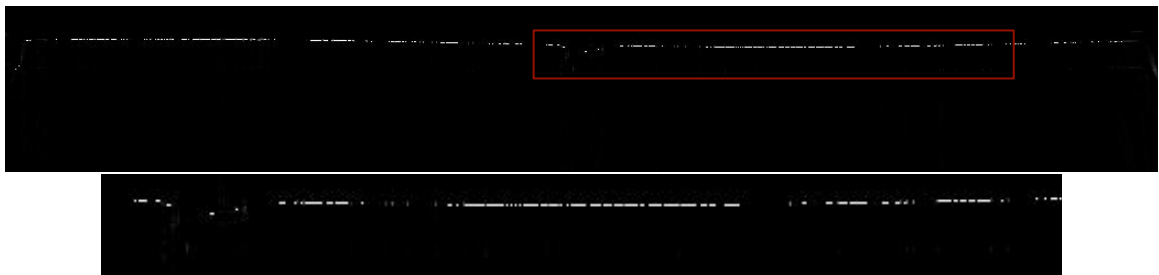


Figure 5.11 - New polar image containing in each column either the maximum detected, in the average position of the maximum in the two gradient images, or the data from the original polar image (on the top), with a zoom of the selected area (below).

The created image was then passed through the minimum path algorithm that would find the minimum path that started and ended in the same point of the line and passed through the detected maxima resulting in the segmented laser line (Figure 5.12).



Figure 5.12 - Minimum path resulting from the GAMP algorithm.

The resulting image with the isolated laser line (with 1 pixel width) was then converted again to Cartesian coordinates and the position of each point of the line relatively to the detected center was extracted (**Figure 5.13**).

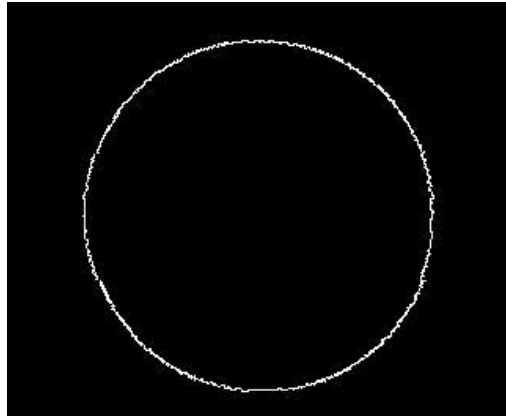


Figure 5.13 - Segmented circular laser line resulting from the MIMP algorithm.

5.2 - Results

To analyse the results obtained with the developed algorithms one cylinder was measured using a calliper ruler and then scanned by the developed scanning system. A 150 mm scan was performed with a step between each image of 5 mm. All the images acquired were processed and the results compared to the ground truth of each image that was marked by a human expert and to a circle generated with the dimensions gathered from the manual measurements of the object. To calculate the errors of the results the Hausdorff distance [56] was used.

To mark the ground truth the user marked as many points as possible in the geometrical center of the laser line, approximately equally spaced, using the isolated red component of each image.

The results were presented in **Tables IV, V, VI, VII and VIII** being the Virtual Image the result of the developed algorithm, the Real Image (**Figure 5.14**) the image generated using the measurements performed with the calliper ruler, and GT the ground truth (**Figure 5.15**) marked by the human expert on the images acquired. The maximum error was considered to be the maximum error obtained in every image acquired, and the average error was the mean of all the calculated errors of the acquired samples. 62 images were analysed for a complete scanning routine of 150 mm length of a dark grey PVC cylinder with 121.2 mm diameter.

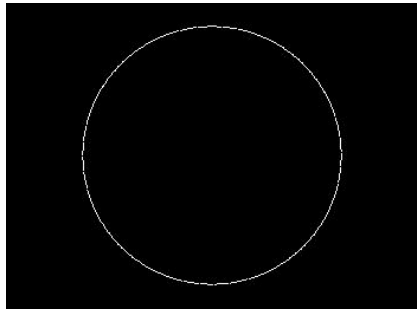


Figure 5.14 - Real Image (circular line generated with the results of the manual measurements of the object).

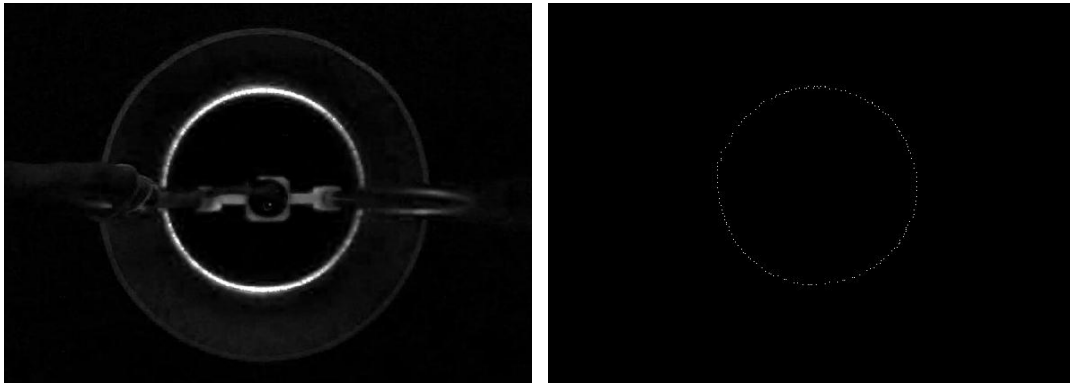


Figure 5.15 - Image in which the ground truth was marked (left) and marked ground truth (right).

All the images acquired were processed by two algorithms in the same computer: iMac 21,5' with a 2.7 GHz Intel Core i5 processor, 8 GB RAM memory (1333 MHz DDR 3) and Mavericks (10.9.3) Operating System. The conversion of pixels to mm, was performed accordingly to the results of the calibration procedure explained in Chapter 6.

The MIMP algorithm presented better results when compared to the Real Image (Table IV) with a maximum segmentation error of 5.66 mm and an average error of 1.46 ± 0.45 mm, while the GAMP algorithm presented a maximum segmentation error of 6.21 mm and an average error of 1.55 ± 0.49 mm.

Table IV: Segmentation error relatively to the real image

Method	Maximum Error Real to Virtual (pixel/mm)	Average Error Real to Virtual (pixel/mm)	Maximum Error Virtual to Real (pixel/mm)	Average Error Virtual to Real (pixel/mm)
MIMP	9.22 / 5.12	2.23 ± 0.76 / 1.24 ± 0.42	10.20 / 5.66	2.62 ± 0.82 / 1.46 ± 0.45
GAMP	9.22 / 5.12	2.28 ± 0.81 / 1.26 ± 0.45	11.18 / 6.21	2.79 ± 0.88 / 1.55 ± 0.49

When compared to the marked ground truth the GAMP algorithm presented slightly better results (Table V) with a maximum segmentation error of 5.50 mm and an average error of 1.34 ± 0.15 mm, while the MIMP algorithm presented the same maximum segmentation error of 5.50 mm and an average error of 1.40 ± 0.15 mm.

Table V: Segmentation error relatively to the ground truth

Method	Maximum Error GT to Virtual (pixel / mm)	Average Error GT to Virtual (pixel / mm)	Maximum Error Virtual to GT (pixel / mm)	Average Error Virtual to GT (pixel / mm)
MIMP	7.07 / 3.92	1.51 ± 0.24 / 0.84 ± 0.13	9.90 / 5.50	2.51 ± 0.26 / 1.40 ± 0.15
GAMP	6.32 / 3.51	1.30 ± 0.23 / 0.72 ± 0.13	9.90 / 5.50	2.40 ± 0.26 / 1.34 ± 0.15

The comparison between the Real Image and the marked ground truths (**Table VI**) showed bigger errors than the comparison of both algorithms with either the Real Image or the marked ground truth. A maximum error of 8.62 mm and an average error of 2.43 ± 0.55 mm were obtained. With this was possible to conclude that the geometrical center of the circular laser line was not the best option to get the real dimensions, but instead the brightest points of the line should be searched. The developed algorithms searched for the brightest points on the laser line, which we believed to correspond to the geometrical center of the line, presenting for that reason good results when compared to the real dimensions. When the ground truth was marked by the human expert this marked approximately the geometrical of the laser line, resulting in a greater error when compared to the real dimensions.

Table VI: Error between the marked ground truth and the real image

Maximum Error GT to Real (pixel / mm)	Average Error GT to Real (pixel / mm)	Maximum Error Real to GT (pixel / mm)	Average Error Real to GT (pixel / mm)
14.21 / 7.90	3.97 ± 1.04 / 2.20 ± 0.58	15.52 / 8.62	4.37 ± 0.99 / 2.43 ± 0.55

When comparing the processing times of both algorithms (**Table VII**), the MIMP algorithm was faster with an average processing time of 64.11 seconds per image, against the 93.13 seconds per image of the GAMP algorithm.

Table VII: Algorithm processing time

Method	Average processing time (s) (per image)
MIMP	64.11
GAMP	93.13

After the analysis of the results obtained, one can state that both algorithms performed well with minor errors, however the MIMP algorithm was faster and more accurate than the

GAMP, when comparing the results with the Real Image, so this algorithm was elected as the best option for this work and was the one used from this point on.

There is a difference between the error from Real to Virtual and Virtual to Real (the same with the Ground Truth) that can be explained by the different number of points of Real, Virtual and GT images.

The error between the GT and the Virtual image is smaller than the error between the Real and the Virtual image, which shows that the error is not only caused by the segmentation algorithm but also by the system. Some modifications to the system that could improve the results would be to use a camera with higher resolution, a set composed by a laser and a conic mirror that would produce a thinner line and even reduce the exposure time of the camera in order to reduce the saturation of the laser line in the images and make it look thinner thus reducing its segmentation error.

In order to evaluate the accuracy of the developed algorithm (MIMP) for the purposed application, it was tested with the images acquired (**Figure 5.16**) during a complete scan of a leg prosthesis socket.

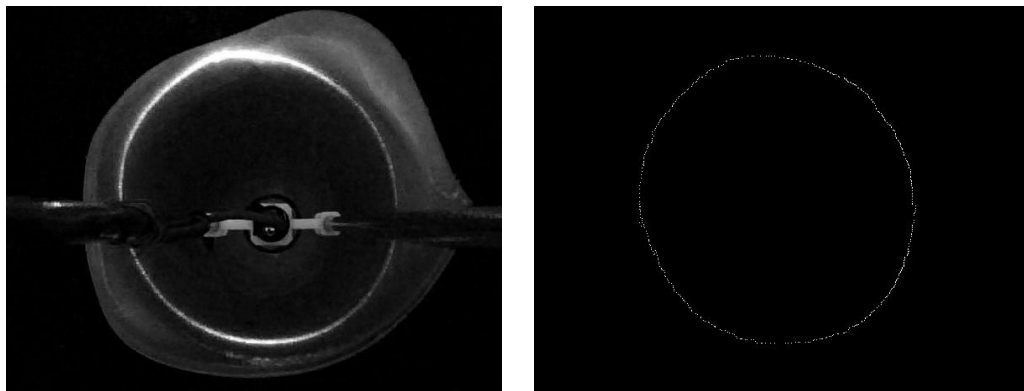


Figure 5.16 - Socket image where the ground truth was marked (left) and marked ground truth (right).

Table VIII: System error relatively to the marked ground truth, in the prosthesis socket

Maximum Error GT to Virtual (pixel / mm)	Average Error GT to Virtual (pixel / mm)	Maximum Error Virtual to GT (pixel / mm)	Average Error Virtual to GT (pixel / mm)
5.83 / 3.24	1.12 ± 0.12 / 0.62 ± 0.06	9.00 / 5.00	1.88 ± 0.17 / 1.04 ± 0.09

For the leg prosthesis socket images the system presents a maximum error of 5.00 mm and an average error of 1.04 ± 0.09 mm when compared to the ground truth marked by the user expert (**Table VIII**).

These results were really promising considering the desired application, once the common variations in the dimensions of the stump during the day are about 10 mm.

Therefore, the reported errors would not compromise significantly the real application of the system to the 3D modelling of a leg prosthesis socket.

5.3 - Summary

Two algorithms were devised and implemented for segmentation of the line resulting from the laser projection.

Both presented good results in face of the desired application, but the MIMP proved to be faster and more accurate, thus being chosen to be used in the continuation of this work for the generation of the 3D models.

Although some modifications can be made both in the system and in the MIMP algorithm to improve the results, the error obtained is within the acceptable range if this system was to be used in 3D modelling of leg prosthesis sockets of real patients as the dimensional variation of the stumps is in the centimetres range.

Chapter 6

System Calibration and Characterization

This chapter shows how the developed laser scanning system was calibrated, by describing the followed methodology and used technics, and presenting the obtained results, and associated conclusions. A complete characterization of the system is also presented.

6.1 - System Calibration

6.1.1 - Methodology

To calibrate the system a grid with 1cm x 1cm squares was printed and placed at the same distance of the camera, as the projected circular laser line, as shown in the first picture in **Figure 6.1**. The grid was aligned and levelled to avoid distortion caused by the paper sheet deformation. Then, images of the grid were acquired with the camera of the system.

The images acquired were manually analysed by the human expert and recurring to Matlab tools to determine the number of pixels between each consecutive corner of a square in different zones of the grid to ensure that there was no radial distortion (**Figure 6.1**).

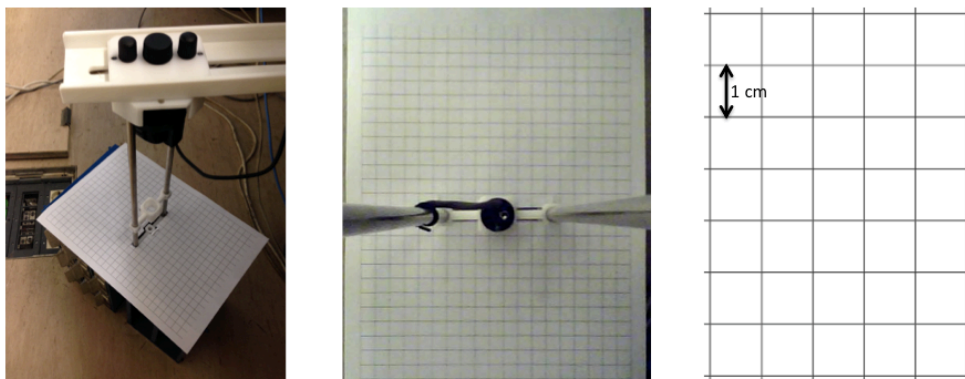


Figure 6.1 - Setup used for calibration of the system (left), grid image acquired with the system camera (center) and a zoomed scheme of the used grid (right).

After obtaining the relation between pixels and the real world dimensions (pixel to cm), random points at different known distances from the center of the system's movement axis were marked on a sheet of paper. That sheet was then placed in the same position as the calibration grid and the images were acquired. The acquired images were manually analysed by the human expert using Matlab tools to evaluate if the calibration was correctly performed (**Figure 6.2**).

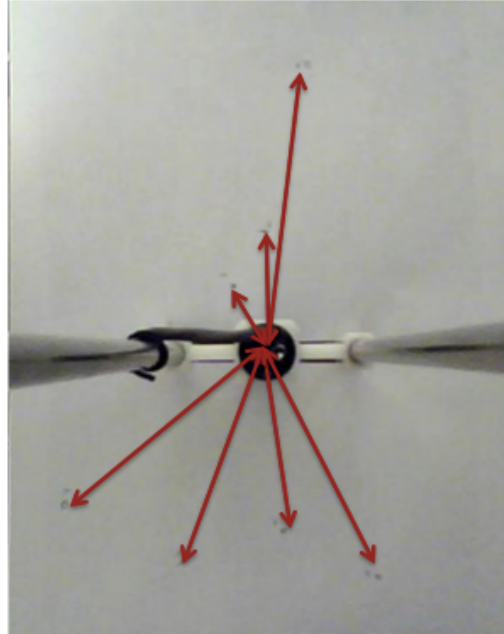


Figure 6.2 - System calibration evaluation.

6.1.2 - Results

The calibration showed that one centimeter (1 cm) in real world corresponded to eighteen pixels (18 pixel in mean) in the image acquired, independently of the location in the image (**Figure 6.3**). Hence, with this experiment it was confirmed that there was no evident radial distortion in the images acquired by the system's camera.

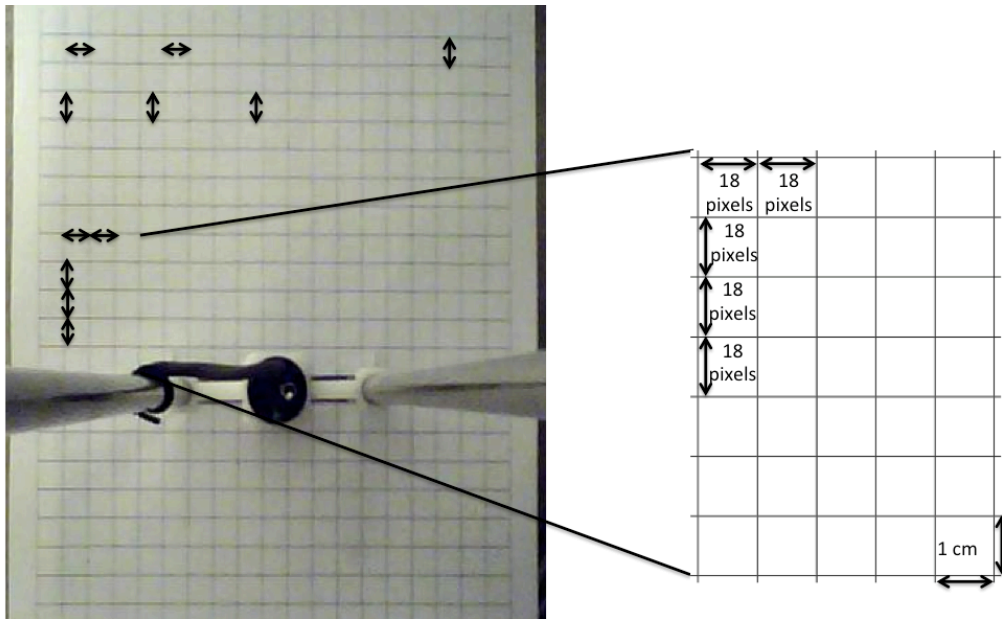


Figure 6.3 - Data used to perform the system calibration, with the scheme of an inset on the right.

The verification of the calibration procedure presented good results, with an average absolute error (Eq. 1) of 1.09 mm and an average relative error (Eq.2) of 1.58%. The error was determined for each marked point by comparing the real distance of the marked point with that determined by the system calibration from the image acquired, and then calculated the average of all errors.

$$\text{Absolute Error} = \text{Virtual Value} - \text{Real Value} \quad (\text{Eq.1})$$

$$\text{Relative Error} = \frac{\text{Virtual Value} - \text{Real Value}}{\text{Real Value}} \times 100 \quad (\text{Eq. 2})$$

6.2 - System Characterization

To perform the system characterization tests, a black cone with known shape was used as the object of analysis (Figure 6.4).



Figure 6.4 - Dark cone with a diameter between 80 and 130.5 mm, used for the system characterization tests.

The acquired images for the different tests were all processed by the developed and previously explained MIMP algorithm, in order to segment the circular laser line.

6.2.1 - Linearity

To perform this test, an algorithm to move the system with a known z-step until a certain point and then again to the starting point was developed, and Matlab “regionprops” was used to determine the average diameter of the object of interest on the acquired image (the same in Resolution and Reproducibility tests). For each step an image was acquired, analysed and the diameter was determined.

In Figure 6.5 the results obtained for this test are presented.

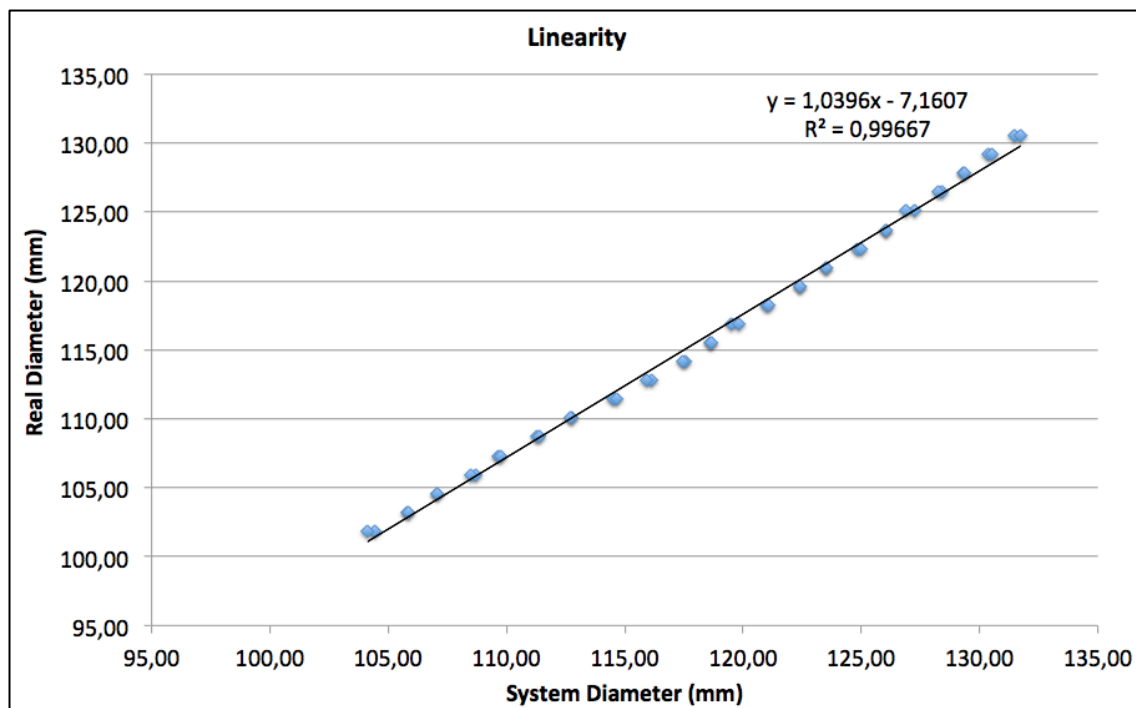


Figure 6.5 - System linearity graph.

It was possible to conclude that the linearity of the results was good with a coefficient of determination (R^2) of 0.9967.

4.3.2 - Resolution

To evaluate the resolution of the system, one hundred consecutive measurements, with an interval of 2 s between them, were made in the same z-position of the cone. After those

measurements, the system was moved to another z-position of the cone and the previous process was repeated.

The achieved results can be seen in **Table IX** and **Figure 6.6**.

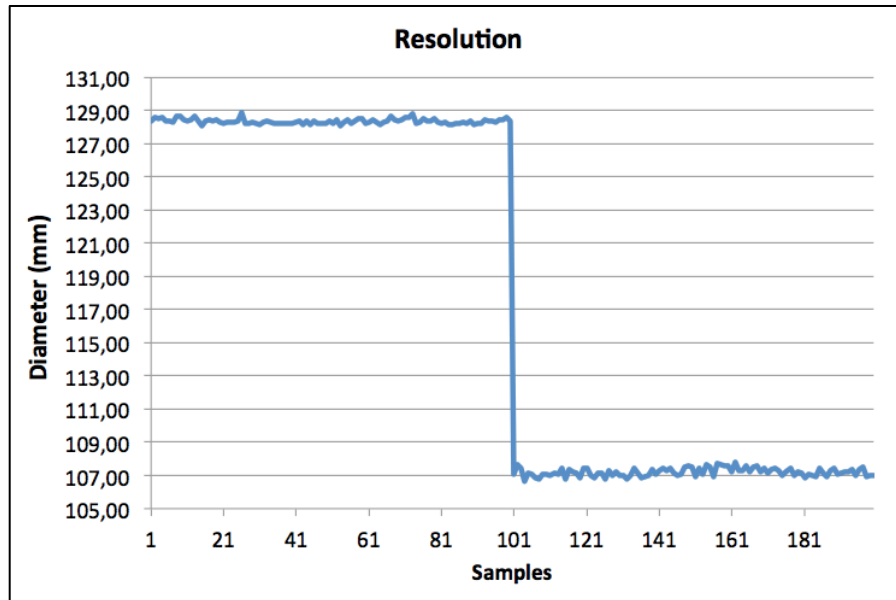


Figure 6.6 - System resolution graph.

Table IX: Results for system resolution

Average [1;100]	128.33 mm	Average [101;200]	107.20 mm
Standard-deviation (σ_1)	0.152	Standard-deviation (σ_2)	0.247

From the previous data (**Table IX**) it was possible to determine the system resolution, as shown below:

$$\text{Resolution} = 2 \times \max(\sigma_1, \sigma_2) = 0.494 \text{ mm}$$

Since the determined dimension of a single pixel was approximately 0.556 mm, we can assume that the maximum resolution achievable with the system would be that of the optical system, which corresponds to a pixel.

4.3.3 - Reproducibility

In this test the system acquired results from the cone during six consecutive hours, in two known z-positions of the cone, during 600 s in each of those positions. Every 6 s, an image of the cone was acquired, and then analysed using the same methodology of the two previous tests.

This test intended to evaluate the immunity of the system to variations of the conditions under which the system was operating, such as the environment illumination, vibrations and component fatigue.

As it is possible to observe in **Figure 6.7** the system presents a good reproducibility, once the determined values were consistent during the entire trial (more detailed results in **Table X** and **Table XI**).

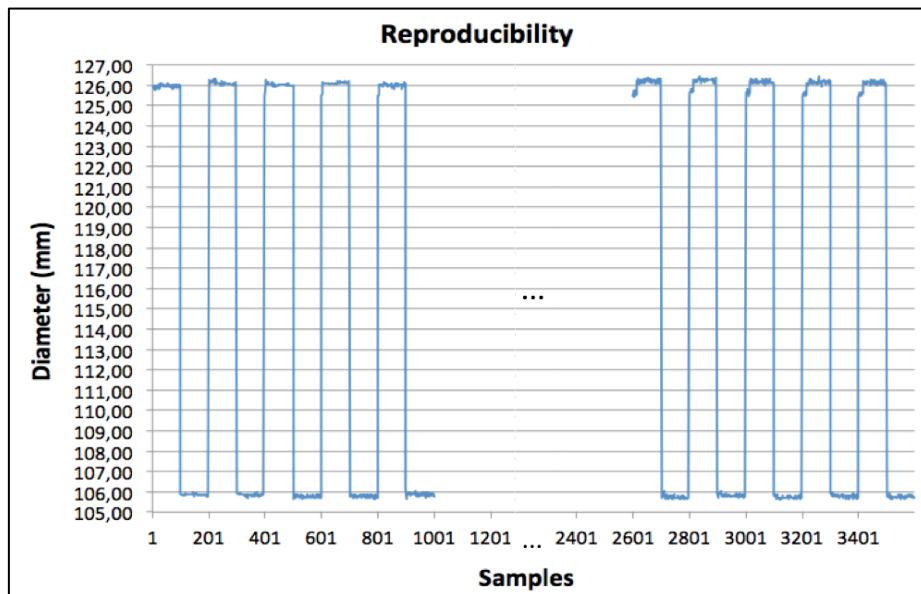


Figure 6.7 - System reproducibility graph.

Table X: Results of system reproducibility on the first 1000 samples

Interval	Average (mm)	Standard-deviation	Interval	Average (mm)	Standard-deviation
[1;100]	125.96	0.07	[501;600]	105.76	0.07
[101;200]	105.86	0.04	[601;700]	126.08	0.12
[201;300]	126.10	0.09	[701;800]	105.08	0.06
[301;400]	105.86	0.04	[801;900]	125.99	0.12
[401;500]	126.02	0.09	[901;1000]	105.87	0.08

Table XI: Results of system reproducibility on the last 1000 samples

Interval	Average (mm)	Standard-deviation	Interval	Average (mm)	Standard-deviation
[2601;2700]	126.15	0.24	[3101;3200]	105.72	0.06
[2701;2800]	105.75	0.09	[3201;3300]	126.05	0.23
[2801;2900]	126.18	0.21	[3301;3400]	105.80	0.08
[2901;3000]	105.81	0.07	[3401;3500]	126.02	0.22
[3001;3100]	126.08	0.21	[3501;3600]	105.76	0.07

4.3.4 - Accuracy

In this experiment the z-position of the system inside the cone was varied with random displacements between 0 mm and 100 mm in both directions (up and down), as in **Figure 6.8**.

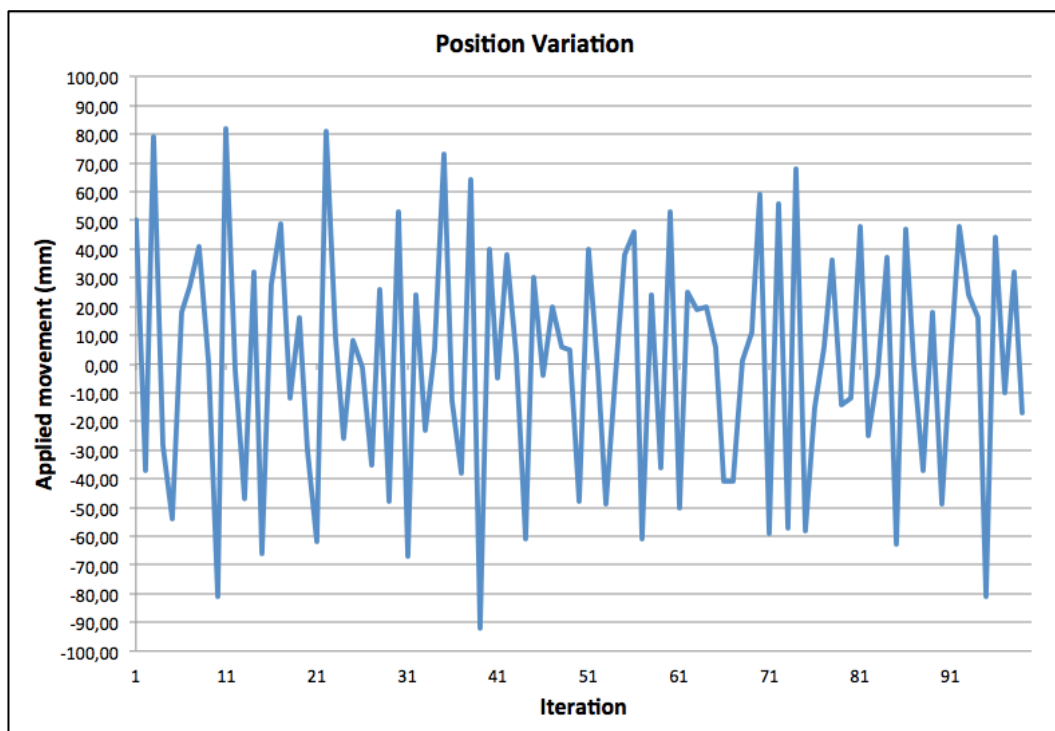


Figure 6.8 - Variation of the z-position of the system inside the cone for the accuracy test.

For each displacement an image was acquired and processed. For each image the result from the system was compared through the Hausdorff Distance [56] with the image generated from the real dimensions of the object, and the associated error was obtained.

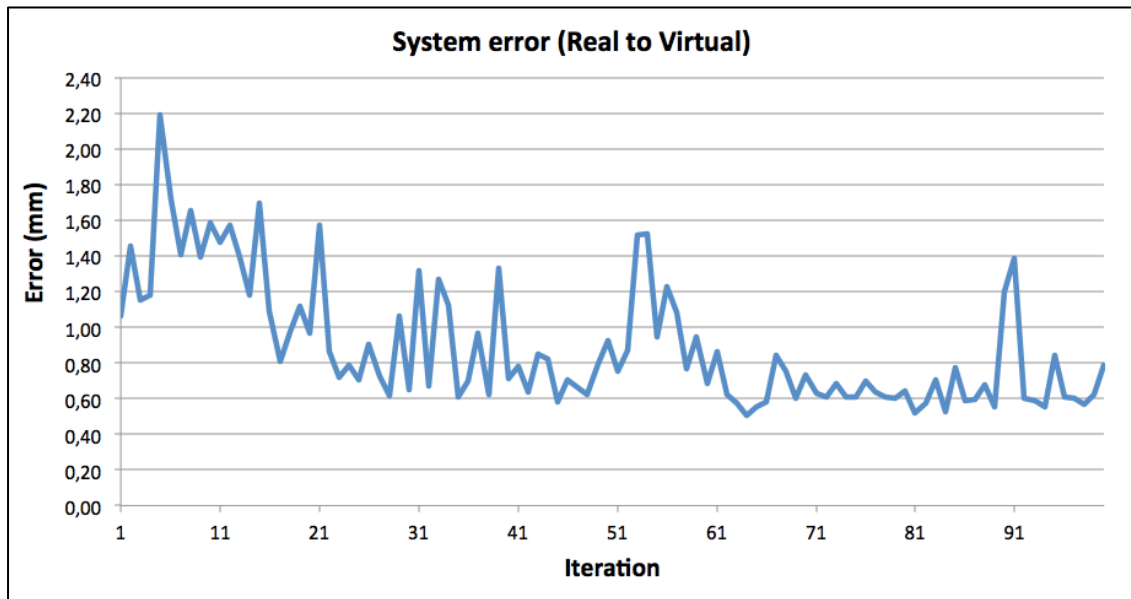


Figure 6.9 - Error (Real to Virtual) obtained for the acquired images for the random dislocations of the system.

By analysing the results obtained (Figure 6.9), between the Real image and the Virtual image, it was determined that for the displacement interval that was considered the maximum error was 2.19 mm and the average error was 0.90 mm with a standard-deviation of 0.35.

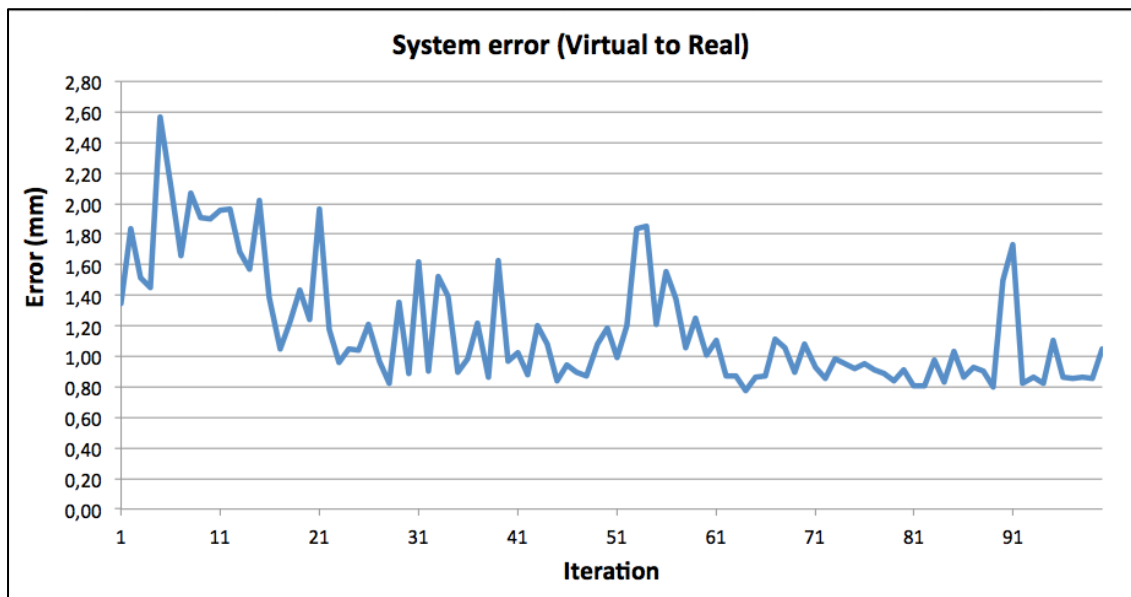


Figure 6.10 - Error (Virtual to Real) obtained for the acquired images for the random dislocations of the system.

By analysing the results obtained (Figure 6.10), between the Virtual image and the Real image, it was determined that for the displacement interval that was considered the

maximum error was 2.56 mm and the average error was 1.19 mm with a standard-deviation of 0.39.

These results showed that the system presented a good accuracy.

4.3.5 - Movement Accuracy

In this experiment the position of the system was randomly varied in a range of ± 200 mm (Figure 6.11).

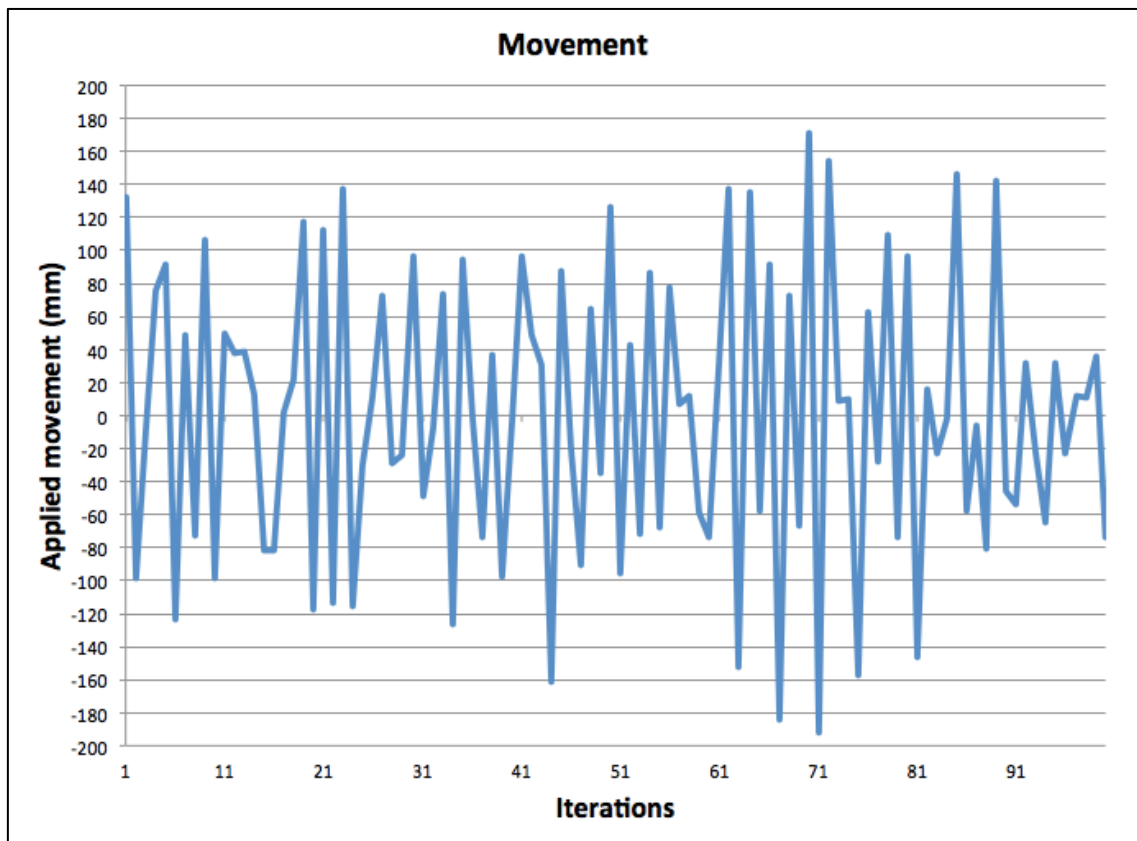


Figure 6.11 - Variation of the z-position of the system for the movement accuracy test.

For each movement the z-position of the system was manually determined (Figure 6.12). For each movement, the value indicated by the system (commanded movement) was compared with the value measured in the precision ruller by the user (performed movement).

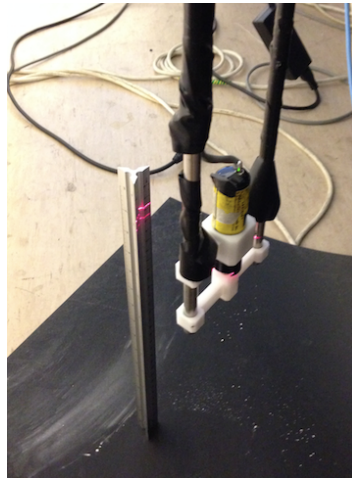


Figure 6.12 - Experimental assembly with the system and the used precision ruler for the movement accuracy test.

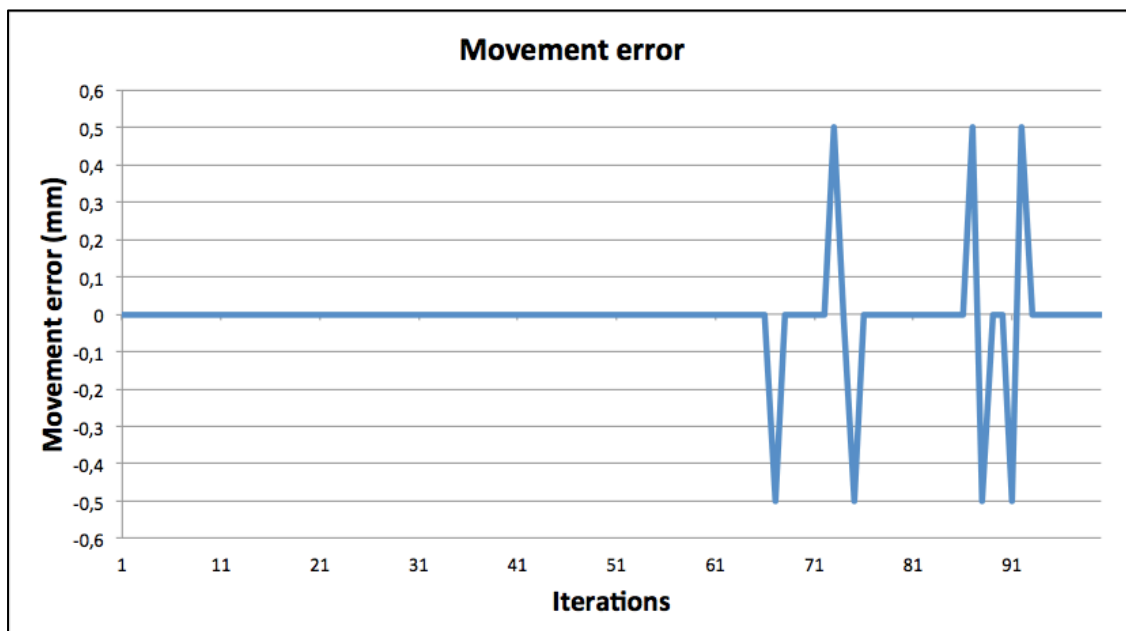


Figure 6.13 - Movement error on the performed random system movements.

As showed in Figure 6.13, it was possible to determine that for movements of ± 200 mm the maximum error was 0.5 mm and the average error was 0.005 mm with a standard-deviation of 0.133.

The results obtained showed that the developed system has an excellent movement accuracy, with a small error.

6.3 - Summary

The calibration of the system showed that 10 mm in real world corresponded to 18 pixels in the images acquired and that there was no evidence of radial distortion in the images acquired with the camera. The calibration yielded an average absolute error of 1.09 mm and an average relative error of 1.58%, which are acceptable for the purpose of the system.

A complete characterization of the developed system was performed, showing excellent results, once the system presents all the characteristics needed to perform the laser scanning of the leg prosthesis socket.

Chapter 7

3D Model Reconstruction

This chapter explains the methodology followed to reconstruct the 3D models from the acquired and processed images, as well as the results obtained.

7.1 - Methodology

To reconstruct the 3D models Matlab® and MeshLab were used. After processing the images, and obtaining the corresponding isolated laser lines, the resulting points of each image of the complete scan in the same z-position, in two opposite directions, were merged to fill the gap created by the metal guides in each image.

The (x,y) coordinates of the points extracted from each image were associated to the z-position at which each image was acquired and a [X Y Z] matrix containing the coordinates of all the points of a complete scan was created. Afterwards, this matrix corresponding to the point cloud was exported to a .ply file, so it could be read and visualized by MeshLab.

The object in **Figure 7.1** was scanned and its 3D model was reconstructed following the steps hereafter presented.



Figure 7.1 - Photos from two different views of the PVC dark grey tube with 121.2 mm diameter that was used in the scanning experiments.

The first step in the MeshLab software was to import the generated Point Cloud (**Figure 7.2**).

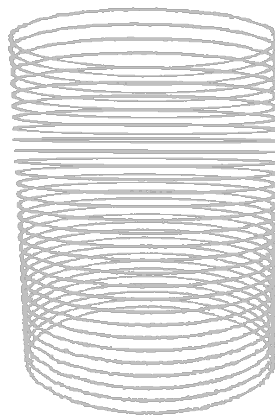


Figure 7.2 - Point Cloud representing the scanned tube, visualized in MeshLab.

After importing the point cloud, the normals on the samples created need to be calculated so that MeshLab knows which side of the point will be facing outside and which will be facing inside. With the normal determined it was finally possible to reconstruct the surface, which has an associated polygonal mesh. The mesh will be created using the tool “Surface reconstruction: Poisson” resulting in the 3D model of the scanned object, formed by a triangular mesh (**Figure 7.3**).

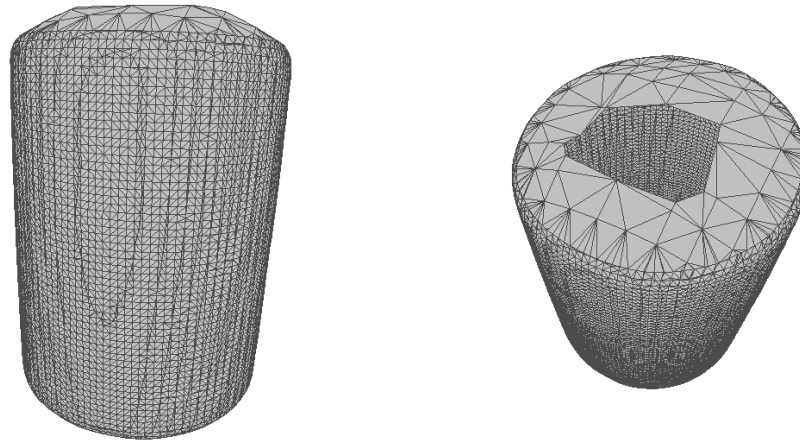


Figure 7.3 - Two different views of the initial 3D model (unedited triangular mesh) of the tube represented in **Figure 7.1**.

The last step was cleaning and adjusting the model, by eliminating excessive faces (**Figure 7.4**).

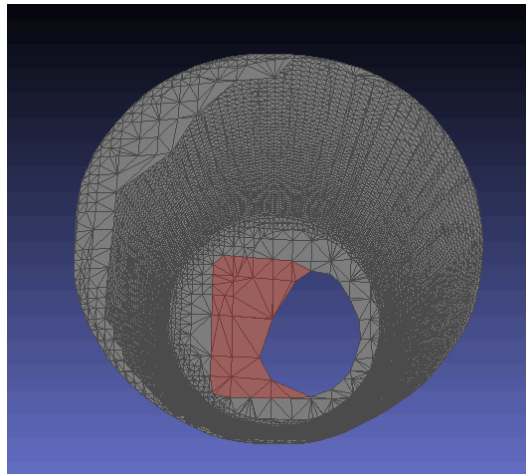


Figure 7.4 - Triangular mesh edition (faces erasing) in MeshLab.

7.2 - Results

In **Figure 7.5** it is possible to see the resulting 3D model from the 3D scanning of the tube in **Figure 7.1** by the developed Laser Scanning System.

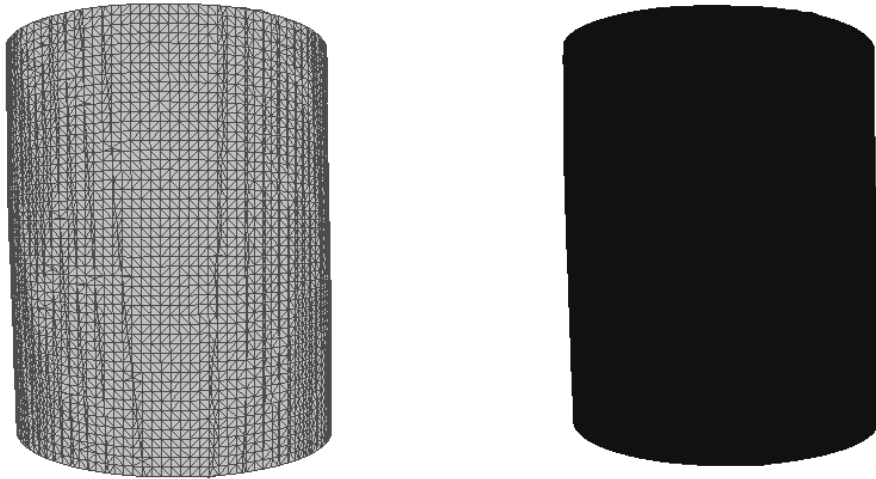


Figure 7.5 - 3D models resulting from the system measurements: triangular mesh model and solid model.

In **Figure 7.6** it is presented the 3D model created with the performed manual measurements of the same object (**Figure 7.1**).

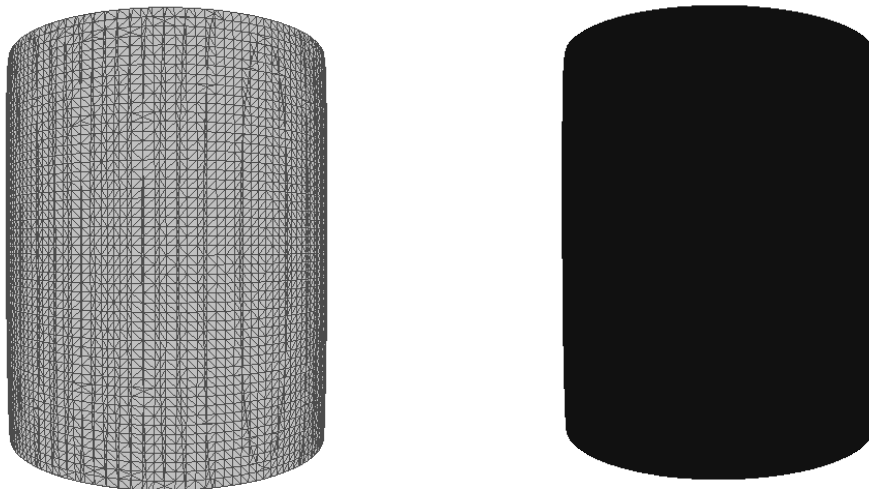


Figure 7.6 - 3D models resulting from the manual measurements: triangular mesh model and solid model.

As shown in the previously presented figures, the produced models show a good resemblance with the original object and with the models created from the manual measurements of the objects.

A scan of a prosthesis socket (**Figure 7.7**) was also performed, and the correspondent 3D model was created (**Figure 7.8**).



Figure 7.7 - Photos from two different views of the socket used to test the 3D laser scanning system.

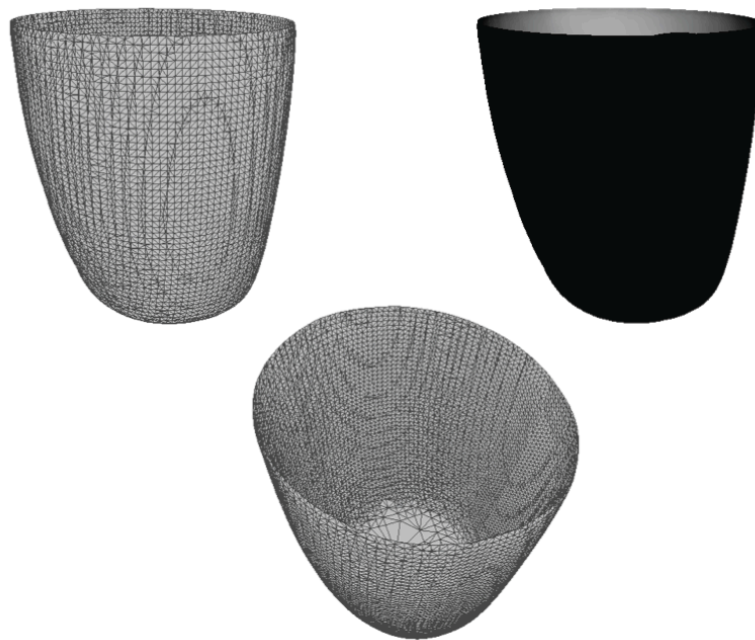


Figure 7.8 - 3D model of the scanned socket, in grey the triangular mesh from two different views and in black the solid model.

The resulting 3D models of the leg prosthesis socket, although they only consider the fully closed part of the socket, also presented a good similarity with original object, which showed great indications of the use of the developed system for the purposed application.

7.3 - Summary

To generate the 3D model of the scanned objects a point cloud was created in Matlab and then imported to MeshLab where the mesh was created and the 3D model finalized.

The resulting 3D models of the performed scans show great resemblance with the interior of the original objects proving the quality and adequacy of the developed solution to the needs of the proposed task.

Chapter 8

Conclusions

The adaptation between the amputee and its prosthesis socket is a complex problem, despite of the type of prosthesis - from the more basic to the more technological - or the amputation level, and it is shared by almost every amputee in the world.

Nowadays the most common method used to build and evaluate the socket adaptation is manual, highly subjective and variable. Some technological aid has been introduced in the latest years, but mostly for the prosthesis design.

There are lots of methods to perform 3D modelling, but most of them are for external parts/surfaces, like the ones used for the 3D modelling of the residual limb in order to perform a guided prosthesis design.

Laser scanning as a method to perform 3D measurements presents good resolution and all the features required to adapt it to the problem under study.

During this work a system to perform laser scanning of the inner surface of prostheses was developed, as well as an electronic circuit to allow the control of a step motor using a computer allowing the movement of the system along the z axis. An algorithm was developed to control the system with Matlab, and easily perform complete scans.

Different algorithms to segment the circular laser line were also developed and optimized, and the results obtained were used to create point clouds that could be exported, edited, manipulated and visualized with specific 3D mesh processing software, such as MeshLab.

The developed system presented good results with small errors, with the final 3D models showing great similarity to the scanned object and to the 3D model generated with the manual measurements performed by a human expert.

In the future, further work should be made to optimize both the system and the developed analysis algorithm, to obtain more accurate results and a more user independent system. The algorithm can also be modified to become more automatic and adaptive to different images from different types of objects. A patient test and the coupling with a

system for the 3D modelling of the amputee stump are already being structured in order to obtain the evaluation of the morphological adaptation between the stump and the socket.

Appendixes

I. Mechanical System Technical Drawings

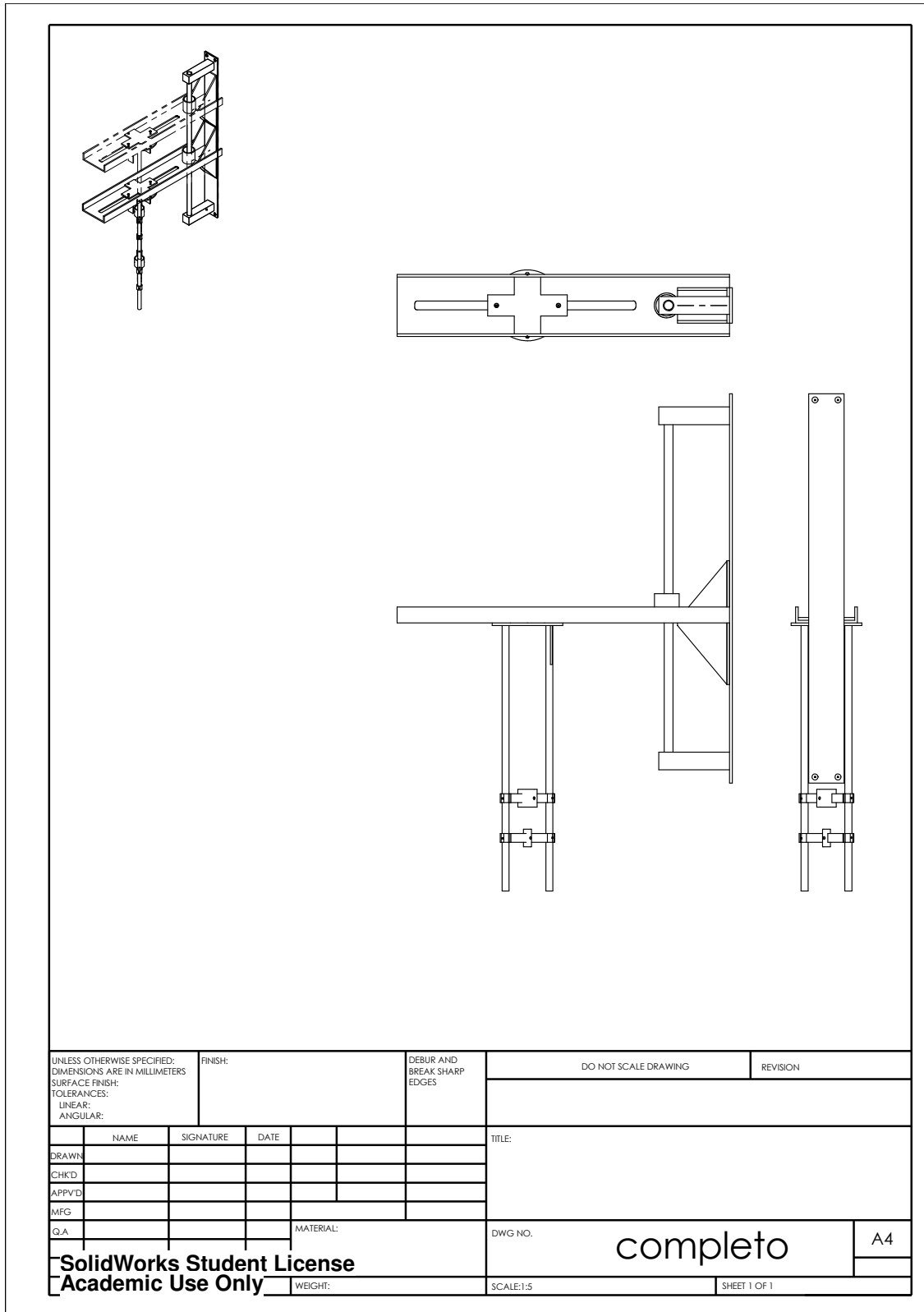


Figure I.1 - Technical drawing of the full mechanical system.

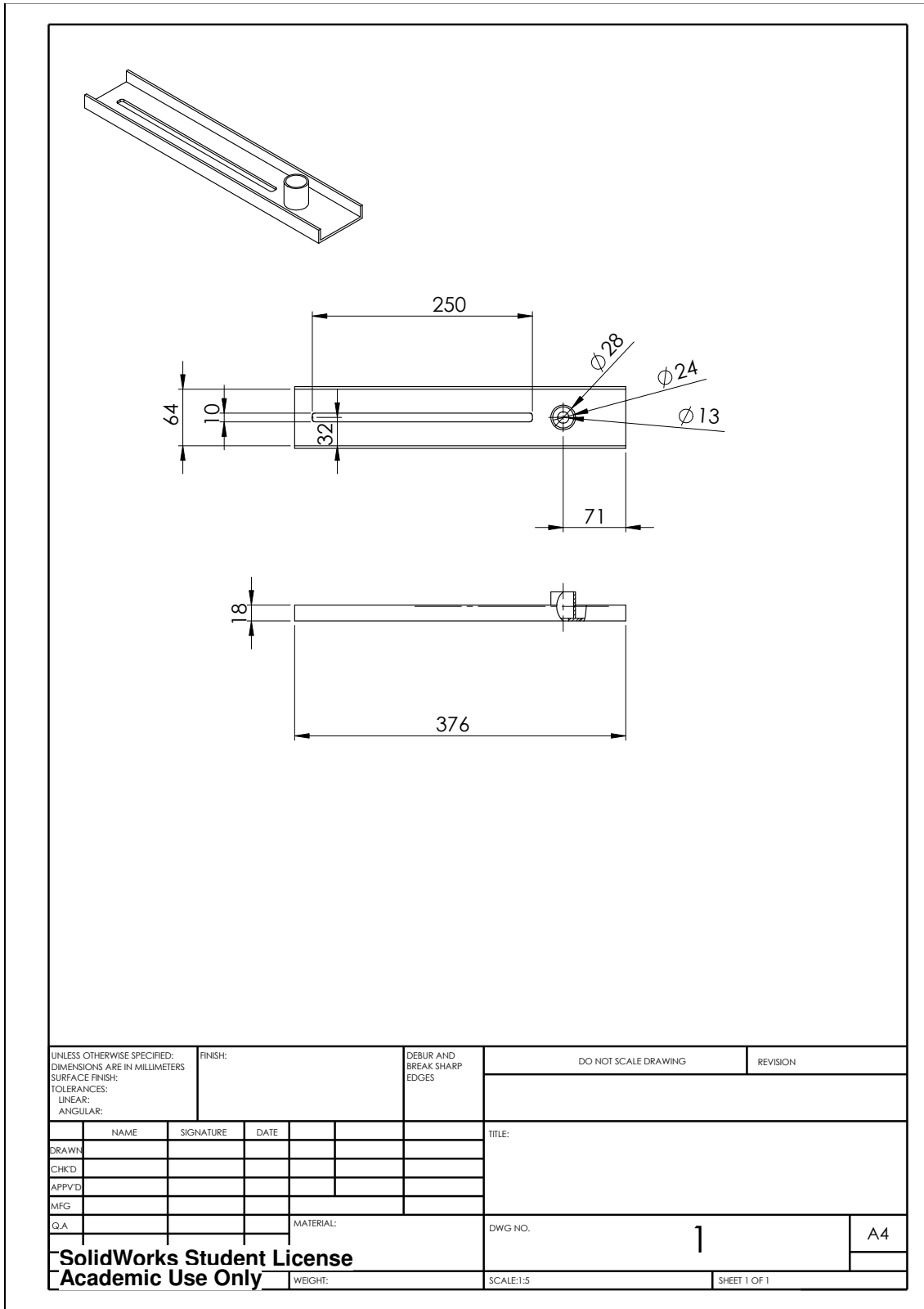


Figure I.2 - Technical drawing of the part that allows the movement along the x axis.

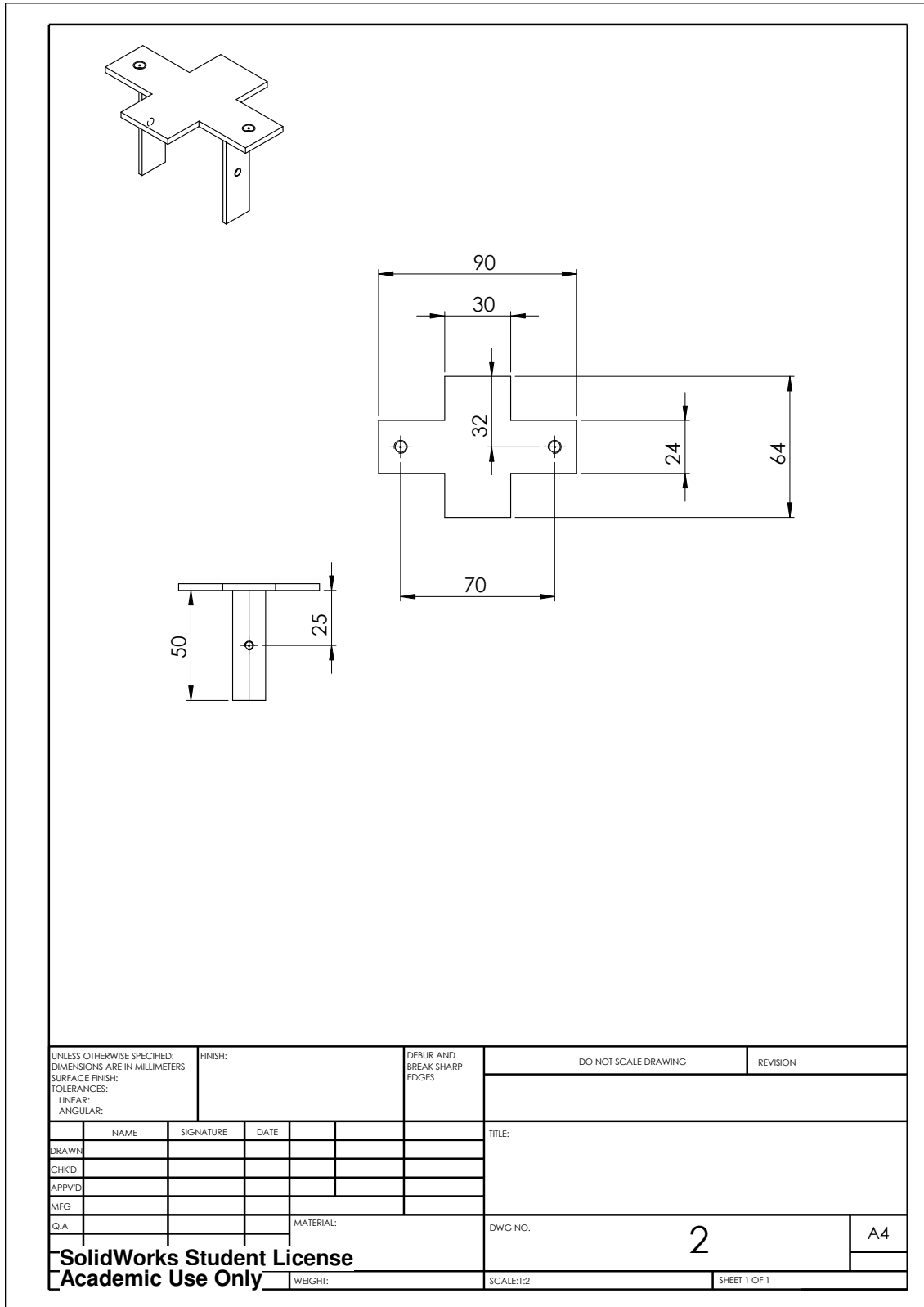


Figure I.3 - Technical drawing of the part that allows the shifting of the camera orientation.

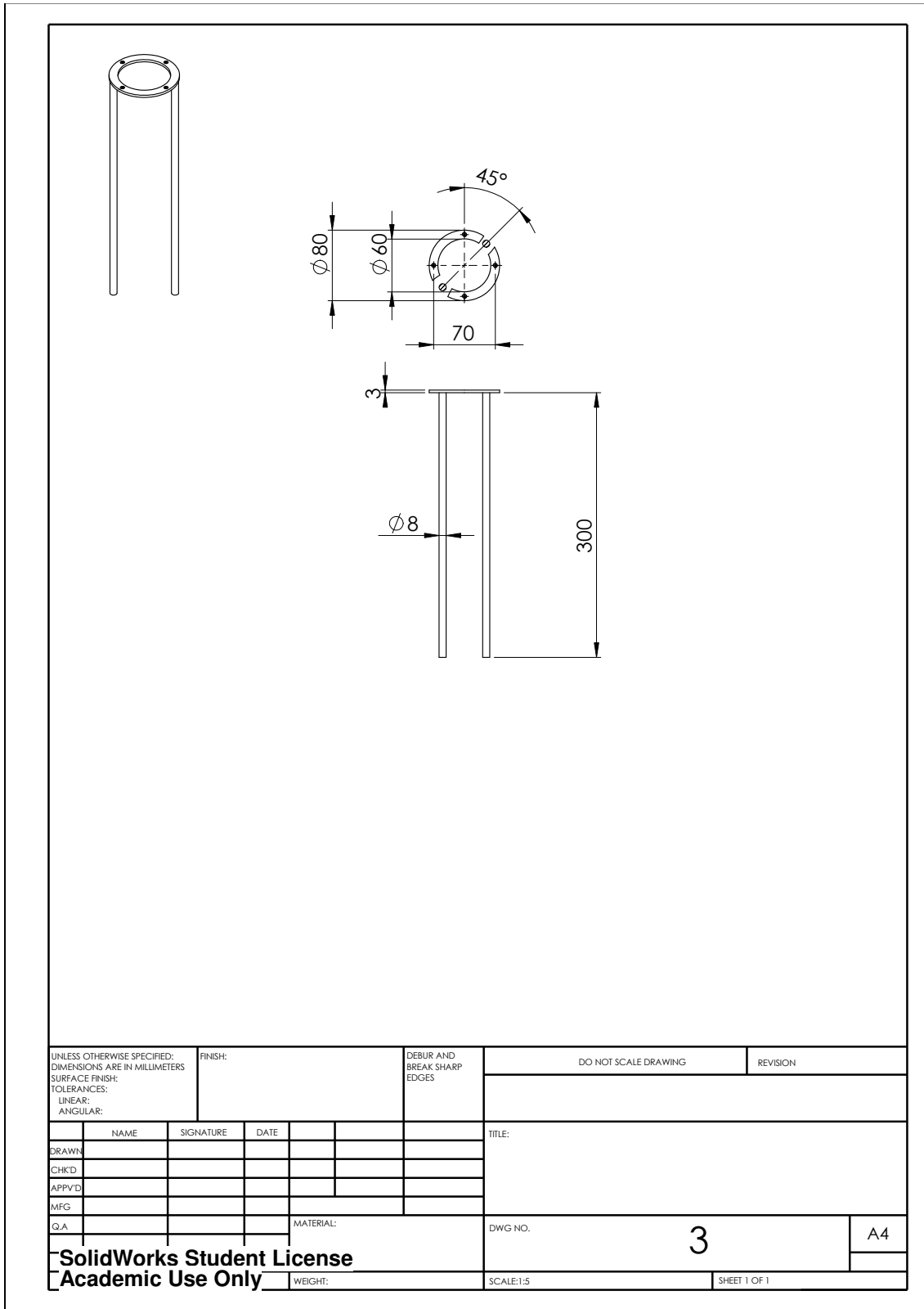


Figure I.4 - Technical drawing of the guiding bars for the movement along z axis.

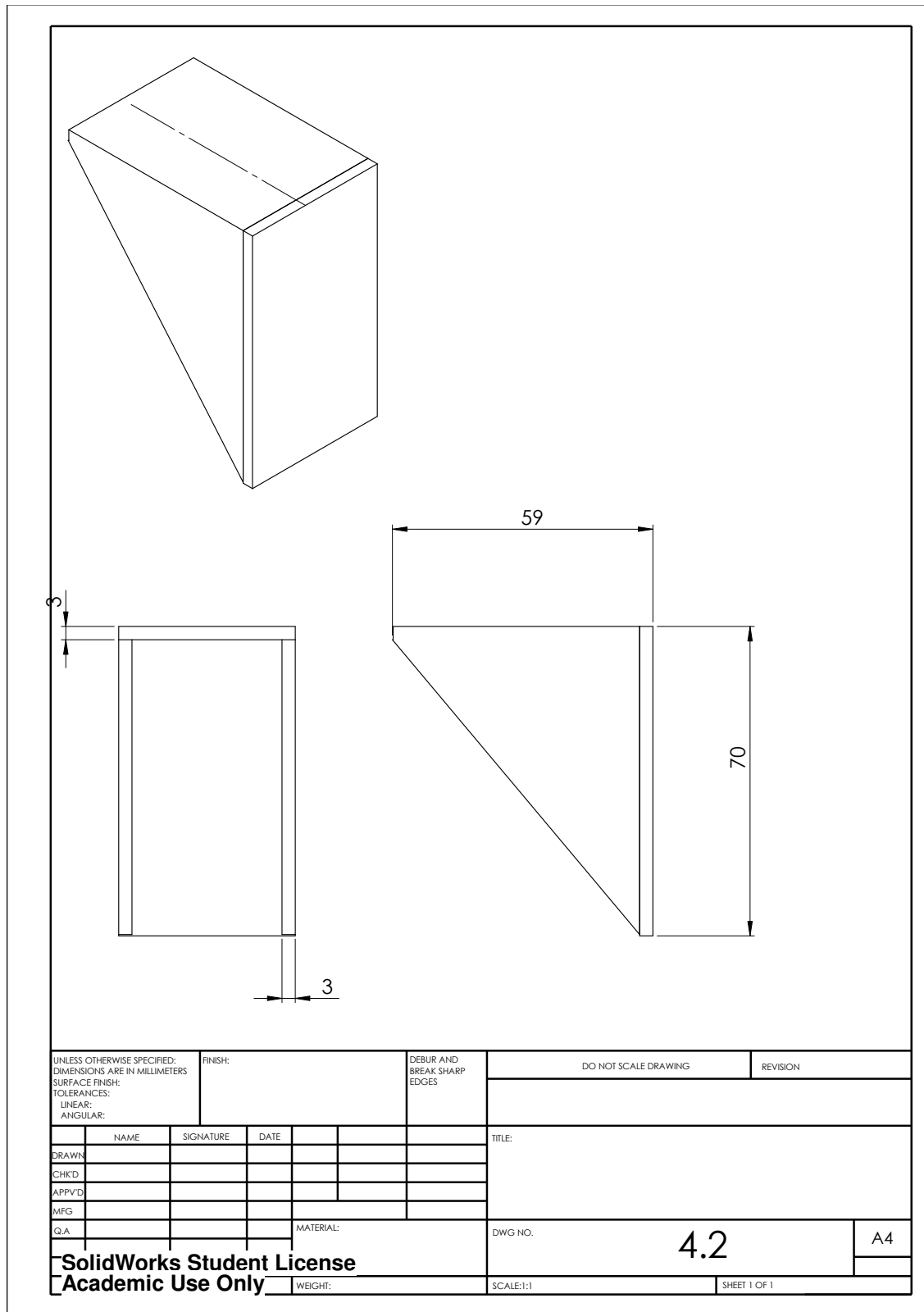


Figure I.5 - Technical drawing of the supporting part.

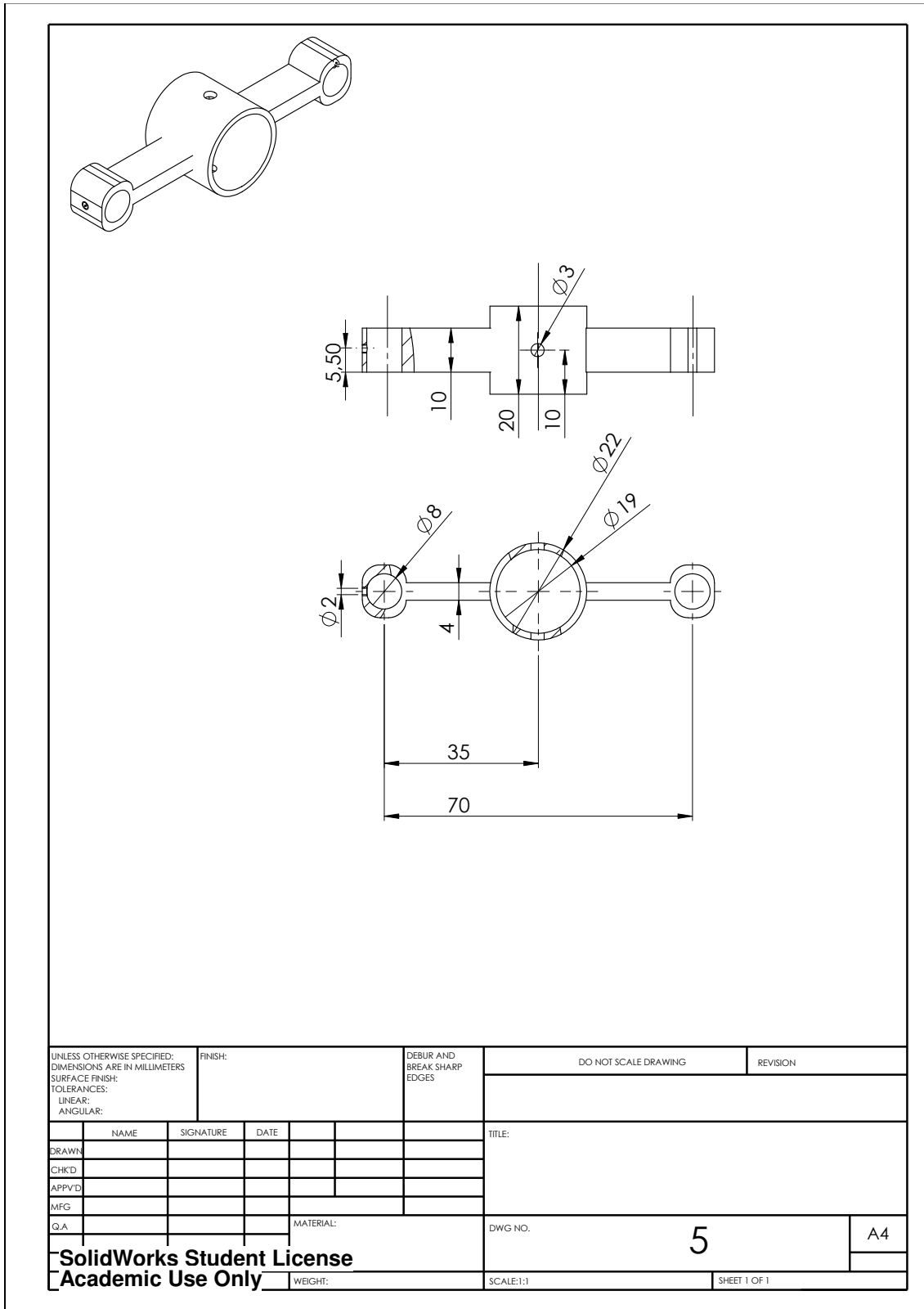


Figure I.6 - Technical drawing of the part that supports the laser.

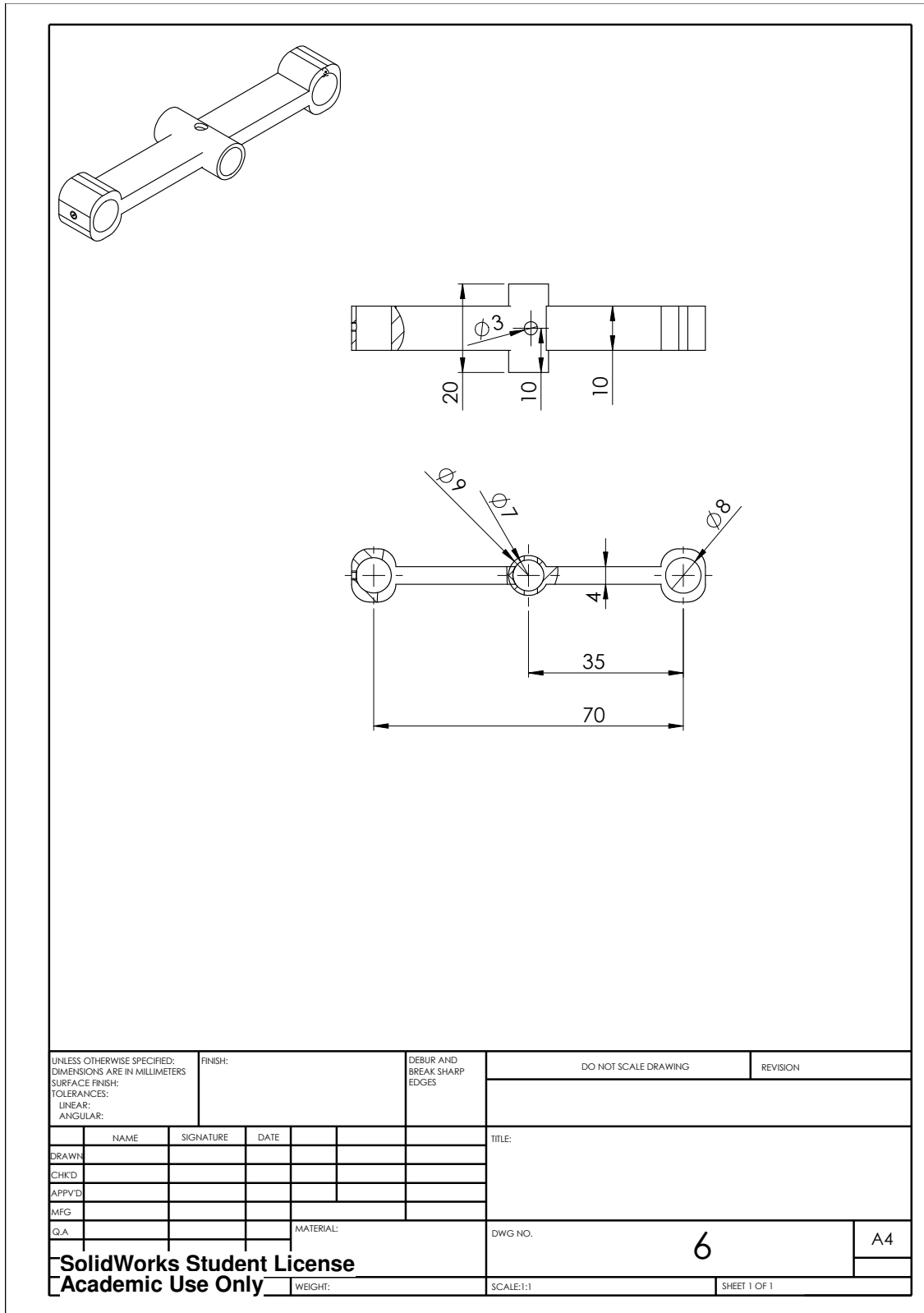


Figure I.7 - Technical drawing of the part that supports the conic mirror.

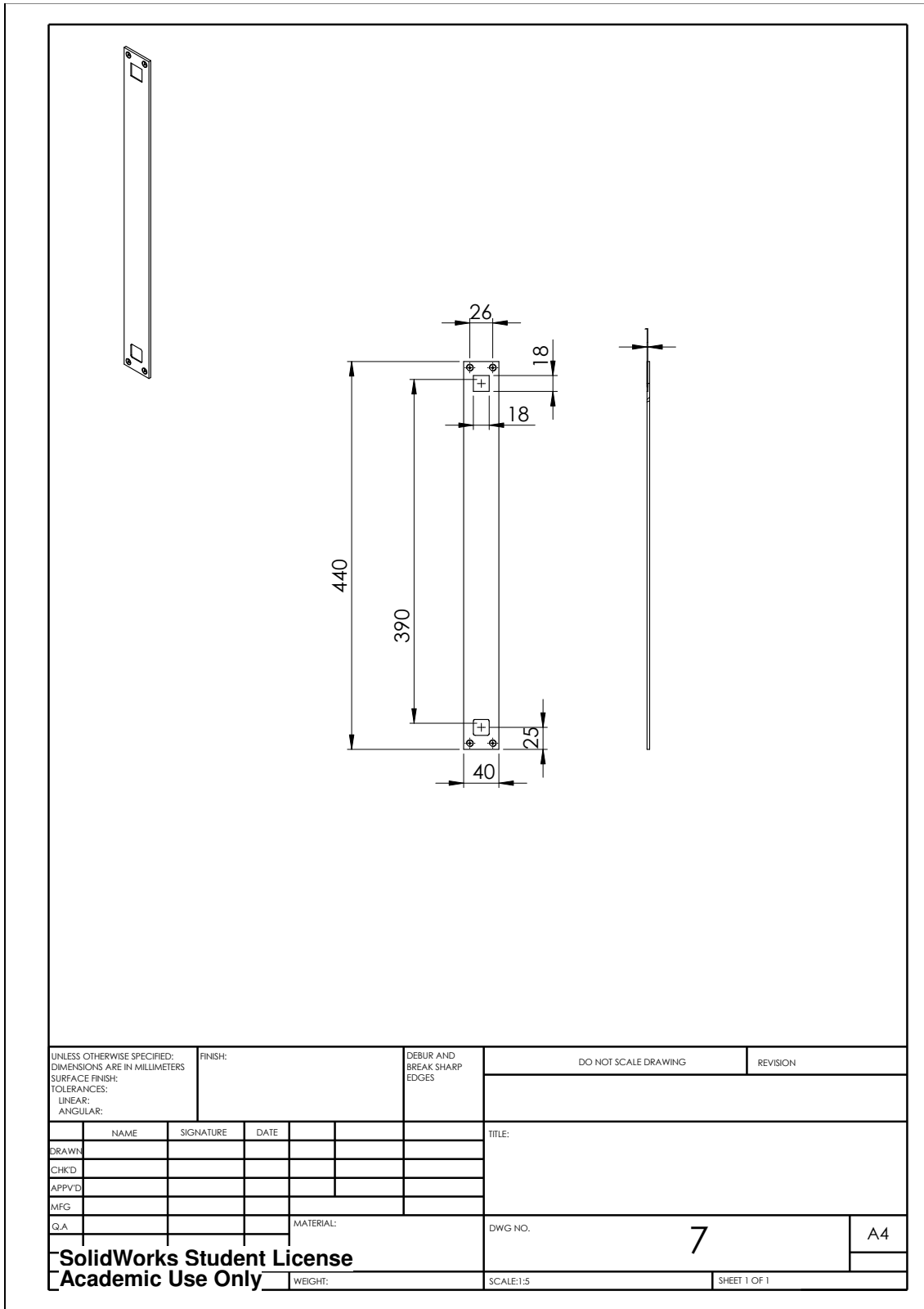


Figure I.8 - Technical drawing of the part that allows the mount of the mechanical system to a vertical surface.

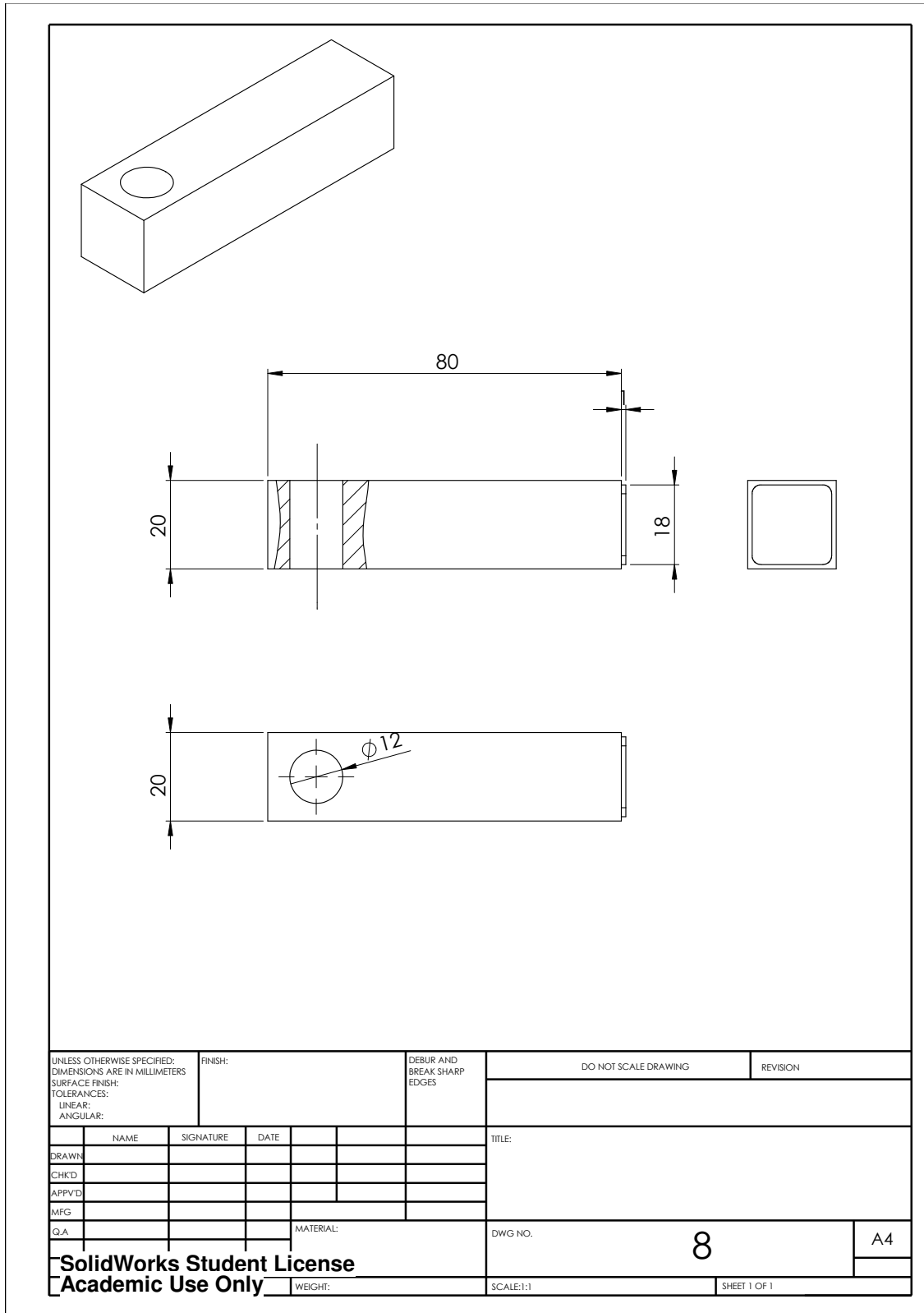


Figure I.9 - Technical drawing of the part that supports the spindle.

II. Electronic Circuit for Step Motor Control

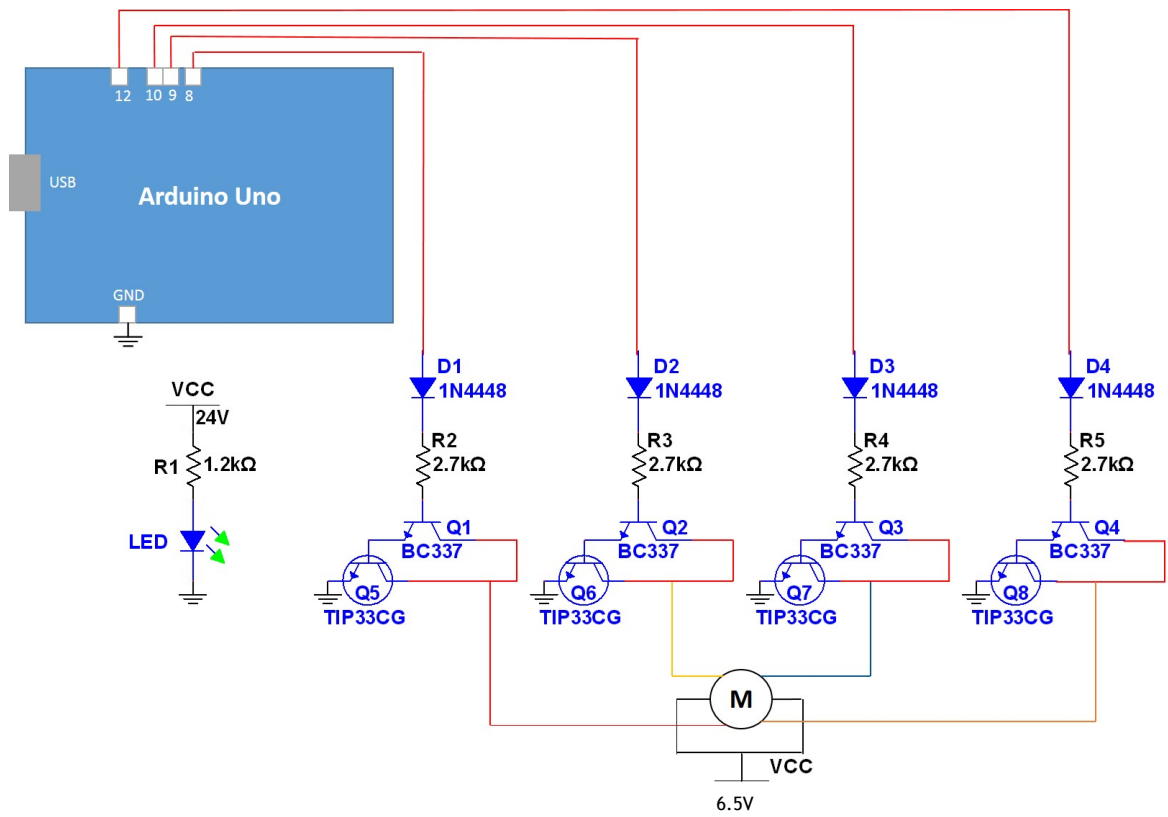


Figure II.1 - Electronic circuit developed for step motor control.

References

- [1] *Dorland's Medical Dictionary for Health Consumers*, 31 ed.: Elsevier, 2007.
- [2] Ottobock. (2014, 29th January 2014). *The Prosthetic Socket*. Available: http://www.ottobock.com/cps/rde/xchg/ob_com_en/hs.xsl/20393.html
- [3] R. Fabio, "From point cloud to surface: the modeling and visualization problem," in *International Workshop on Visualization and Animation of Reality-based 3D Models*, 2003, p. 5.
- [4] A. H. Dictionary and H. M. Company, *The American Heritage Dictionary of the English Language*: Houghton Mifflin Harcourt Publishing Company, 2006.
- [5] E. Mendes, "Alterações da função do Sistema Neuro Músculo Esquelético e os DM externos," ed. Class of Engenharia da Reabilitação (FEUP), 2011.
- [6] G. Facoetti, S. Gabbiadini, G. Colombo, and C. Rizzi, "Knowledge-based system for guided modeling of sockets for lower limb prostheses," *Comput. Aided Design Appl*, vol. 7, pp. 723-737, 2010.
- [7] G. Colombo, G. Facoetti, S. Gabbiadini, and C. Rizzi, "Virtual configuration of lower limb prosthesis," 2010.
- [8] S. Gabbiadini, "Knowledge-based design of lower limb prosthesis," PhD Thesis, Dipartimento di Innovazione Meccanica e Gestionale, Università degli Studi di Padova, 2011.
- [9] M. Janos P. Ertl. (2012). *Amputations of the Lower Extremity*. Available: <http://emedicine.medscape.com/article/1232102-overview>.
- [10] F. Boccolini, "Reabilitação: amputados, amputações e próteses; Rehabilitation: amputee, amputations and prostheses," 1990.
- [11] C. Alves Pereira and J. Henriques, "Cirurgia: Patologia e Clínica. 2ª edição," ed: McGraw Hill Madrid;, 2006.
- [12] D. G. Smith, J. W. Michael, and J. H. Bowker, *Atlas of amputations and limb deficiencies: surgical, prosthetic, and rehabilitation principles*: American Academy of Orthopaedic Surgeons Rosemont, IL, 2004.
- [13] D. F. Matos, "Dispositivos Protésicos Exteriores: Estudo, Desenvolvimento, Produção, Ensaio e Certificação," Master in Industrial Design MSc thesis, Universidade do Porto, FEUP, 2009.
- [14] J. A. Carvalho, *Amputações de membros inferiores: em busca da plena reabilitação*: Manole, 2003.
- [15] C. d. R. P. d. Gaia. (27 December 2013). *Membro Inferior: Encaixes-tipo*. Available: http://www.crbg.pt/solucoes/produtos_apoio/proteses/Paginas/membroinferior.aspx - t3
- [16] Y. V. Chugui, "Optical Measuring Systems and Laser Technologies for Scientific and Industrial Applications."
- [17] J. Salvi, S. Fernandez, T. Pribanic, and X. Llado, "A state of the art in structured light patterns for surface profilometry," *Pattern recognition*, vol. 43, pp. 2666-2680, 2010.
- [18] K. Hasegawa and Y. Sato, "Endoscope system for high-speed 3D measurement," *Systems and Computers in Japan*, vol. 32, pp. 30-39, 2001.

- [19] D. Marr, T. Poggio, E. C. Hildreth, and W. E. L. Grimson, "A computational theory of human stereo vision," in *From the Retina to the Neocortex*, ed: Springer, 1991, pp. 263-295.
- [20] L. Ballan, N. Brusco, and G. M. Cortelazzo, "3D Content Creation by Passive Optical Methods," *3D Online Multimedia and Games: Processing, Visualization and Transmission*, p. 231, 2008.
- [21] F. Magalhães, "Implementação de um sistema baseado em luz estruturada e de um sistema de varrimento laser para obtenção da forma tridimensional da superfície de objectos," FEUP, Reconstrução Assistida de Objectos 3D - RAO3D 14 July 2009.
- [22] F. Magalhães, "Métodos de calibração de câmaras e técnicas baseadas em luz estruturada para caracterização tridimensional da superfície de objectos," FEUP, Reconstrução Assistida de Objectos 3D - RAO3D 7 May 2009.
- [23] A. Turner-Smith, "Structured light surface measurement techniques," *Orr J, Shelton J. Optical measurement methods in biomechanics. Germany: Chapman & Hall*, pp. 39-58, 1997.
- [24] Ø. Skotheim and F. Couwleers, "Structured light projection for accurate 3D shape determination," in *Proceedings of the 12th International Conference on Experimental Mechanics*, 2004, pp. 536-541.
- [25] G. Zhang, J. He, and X. Li, "3D vision inspection for internal surface based on circle structured light," *Sensors and Actuators A: Physical*, vol. 122, pp. 68-75, 2005.
- [26] J. Salvi, J. Pages, and J. Batlle, "Pattern codification strategies in structured light systems," *Pattern Recognition*, vol. 37, pp. 827-849, 2004.
- [27] I. Vite-Silva, N. Cruz-Cortés, G. Toscano-Pulido, and L. G. de la Fraga, "Optimal triangulation in 3D computer vision using a multi-objective evolutionary algorithm," in *Applications of Evolutionary Computing*, ed: Springer, 2007, pp. 330-339.
- [28] G. Sansoni, M. Trebeschi, and F. Docchio, "State-of-the-art and applications of 3D imaging sensors in industry, cultural heritage, medicine, and criminal investigation," *Sensors*, vol. 9, pp. 568-601, 2009.
- [29] P. J. Besl, "Active, optical range imaging sensors," *Machine vision and applications*, vol. 1, pp. 127-152, 1988.
- [30] B. K. P. Horn, *Robot Vision: MIT ELECTRICAL ENGINEERING AND COMPUTER SCIENCE SE: the MIT Press*, 1986.
- [31] S. K. Nayar, M. Watanabe, and M. Noguchi, "Real-time focus range sensor," *Pattern Analysis and Machine Intelligence, IEEE Transactions on*, vol. 18, pp. 1186-1198, 1996.
- [32] H. Hoppe, T. DeRose, T. Duchamp, J. McDonald, and W. Stuetzle, *Surface reconstruction from unorganized points* vol. 26: ACM, 1992.
- [33] J.-D. Boissonnat, "Geometric structures for three-dimensional shape representation," *ACM Transactions on Graphics (TOG)*, vol. 3, pp. 266-286, 1984.
- [34] F. Iselhard, G. Brunnett, and T. Schreiber, *Polyhedral reconstruction of 3d objects by tetrahedra removal: Fachbereich Informatik, Univ.*, 1997.
- [35] B. Curless and M. Levoy, "A volumetric method for building complex models from range images," in *Proceedings of the 23rd annual conference on Computer graphics and interactive techniques*, 1996, pp. 303-312.
- [36] D. Terzopoulos, "The computation of visible-surface representations," *Pattern Analysis and Machine Intelligence, IEEE Transactions on*, vol. 10, pp. 417-438, 1988.
- [37] C. Gotsman and D. Keren, "Tight fitting of convex polyhedral shapes," *International Journal of Shape Modeling*, vol. 4, pp. 111-126, 1998.
- [38] S. Muraki, "Volumetric shape description of range data using "Blobby Model"," in *ACM SIGGRAPH Computer Graphics*, 1991, pp. 227-235.
- [39] D. Moore and J. Warren, "Approximation of dense scattered data using algebraic surfaces," in *System Sciences, 1991. Proceedings of the Twenty-Fourth Annual Hawaii International Conference on*, 1991, pp. 681-690.
- [40] T. K. Dey and J. Giesen, "Detecting undersampling in surface reconstruction," in *Discrete and Computational Geometry*, ed: Springer, 2003, pp. 329-345.
- [41] J. F. Brinkley, "Knowledge-driven ultrasonic three-dimensional organ modeling," *Pattern Analysis and Machine Intelligence, IEEE Transactions on*, pp. 431-441, 1985.

- [42] T. Hastie and W. Stuetzle, "Principal curves," *Journal of the American Statistical Association*, vol. 84, pp. 502-516, 1989.
- [43] M. L. Merriam, "Experience with the cyberware 3D digitizer," in *NCGA Conference Proceedings*, 1992, pp. 125-125.
- [44] M. S. Floater and A. Iske, "Thinning algorithms for scattered data interpolation," *BIT Numerical Mathematics*, vol. 38, pp. 705-720, 1998.
- [45] P. Fua and P. Sander, "Reconstructing surfaces from unstructured 3d points," in *Second European Conference on Computer Vision (ECCV'90)*, 1992.
- [46] N. A. Borghese and S. Ferrari, "A portable modular system for automatic acquisition of 3D objects," *Instrumentation and Measurement, IEEE Transactions on*, vol. 49, pp. 1128-1136, 2000.
- [47] M. Bern and D. Eppstein, "Mesh generation and optimal triangulation," *Computing in Euclidean geometry*, vol. 1, pp. 23-90, 1992.
- [48] J. C. Carr, R. K. Beatson, J. B. Cherrie, T. J. Mitchell, W. R. Fright, B. C. McCallum, et al., "Reconstruction and representation of 3D objects with radial basis functions," in *Proceedings of the 28th annual conference on Computer graphics and interactive techniques*, 2001, pp. 67-76.
- [49] Y.-P. Zheng, A. F. Mak, and A. K. Leung, "State-of-the-art methods for geometric and biomechanical assessments of residual limbs: a review," *Journal of rehabilitation research and development*, vol. 38, pp. 487-504, 2001.
- [50] V. L. Houston, E. M. Burgess, D. S. Childress, H. R. Lehneis, B. Boone, R. B. Chan, et al., "Automated fabrication of mobility aids (AFMA): D progr," 1992.
- [51] D. A. Boone, J. Harlan, and E. M. Burgess, "Automated fabrication of mobility aids: review of the AFMA process and VA/Seattle ShapeMaker software design," *Journal of rehabilitation research and development*, vol. 31, pp. 42-42, 1994.
- [52] S. A. Stefani, C. R. Nagarajah, and D. J. Toncich, "Non-contact inspection for the detection of internal surface defects in hollow cylindrical work-pieces," *The International Journal of Advanced Manufacturing Technology*, vol. 11, pp. 146-154, 1996.
- [53] M. Kass, A. Witkin, and D. Terzopoulos, "Snakes: Active contour models," *International journal of computer vision*, vol. 1, pp. 321-331, 1988.
- [54] H. Oliveira, "An affordable and practical 3d solution for the aesthetic evaluation of breast cancer conservative treatment," Ph.D. Dissertation, Faculty of Engineering of the University of Porto, 2013.
- [55] T. Tuytelaars and K. Mikolajczyk, "Local invariant feature detectors: a survey," *Foundations and Trends® in Computer Graphics and Vision*, vol. 3, pp. 177-280, 2008.
- [56] D. P. Huttenlocher, G. A. Klanderman, and W. J. Rucklidge, "Comparing images using the Hausdorff distance," *Pattern Analysis and Machine Intelligence, IEEE Transactions on*, vol. 15, pp. 850-863, 1993.